Renewable and Sustainable Energy Reviews 150 (2021) 111514

Contents lists available at ScienceDirect

Renewable and Sustainable Energy Reviews

journal homepage: www.elsevier.com/locate/rser

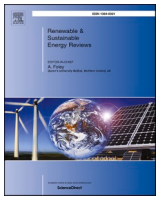

A review on various optical fibre sensing methods for batteries

Gaoce Han [a,b], Jize Yan [b], Zhen Guo [a], David Greenwood [a], James Marco [a], Yifei Yu [a,*]

[a] Warwick Manufacturing Group (WMG), University of Warwick, Coventry, CV4 7AL, United Kingdom
[b] Electronics and Computer Science (ECS), University of Southampton, Southampton, SO17 1BJ, United Kingdom

ARTICLE INFO

Keywords:
Battery sensing
Optical fibre sensors
Batteries
Battery instrumentation
Battery management system
Smart sensing

ABSTRACT

Batteries have rapidly evolved and are widely applied in both stationary and transport applications. The safe and reliable operation is of vital importance to all types of batteries, herein an effective battery sensing system with high performance and easy implementation is critically needed. This also requires the sensing system to monitor the states of batteries in real time. Among the available methods, optical fibre sensors have shown a significant advantage due to their advanced capabilities of which include the fast measurement of multiple parameters with high sensitivity, working without interfering the battery performance, being able to be composited in multiplexed configurations and being robust to various harsh environment conditions. This paper mainly discusses the current optical fibre sensing methods for batteries in terms of the working principles and critical reviews the sensing performance corresponding to different sensing parameters. Moreover, the challenges and outlooks for future research on battery sensing are derived.

1. Introduction

Batteries, as one of the sustainable energy storage technologies [1], have rapidly evolved due to the global issues of energy crisis and air pollution in the last decades. They also are popular in supplying power to consumer electronics such as laptops, tablets, cameras, watches and portable phones. In particular, they are considered to be the ideal power sources in electric vehicles (EVs) and hybrid electric vehicles (HEVs) [2]. Currently, batteries have been widely applied in both stationary and transport applications attributing to their high energy density, long cycle-life, low self-discharge and high safety level. There are diverse battery technologies such as lithium-ion (Li-ion) batteries, lead-acid batteries, flow batteries and high-temperature batteries depending on the battery electrochemistry. According to the research of International Renewable Energy Agency, batteries contributed 1.9 GW (1.1 %) to the installed storage power capacity globally at mid-2017, in which Li-ion batteries dominated total electricity storage power capacity with 59 %, followed by small but important contributions from lead-acid batteries with 3 %, high temperature sodium sulphur batteries with 3 % and flow batteries with 2 %, respectively [3]. It is rapidly expanding and reaching a capacity of 6 GW (5 %) in 2019, in which variants of Li-ion batteries account for 93 % of total annual new energy storage installations and other batteries make up the majority of the remaining 7 % [4]. Driven by optimisation of manufacturing facilities, combined with better combinations and reduced use of materials, the unit cost of batteries for transport applications has already fallen by 85 % since 2010 [4], the total installed cost of batteries could drop 50–66 % by 2030 in stationary applications [3]. With the large cost reduction potential for battery storage technologies and the continued improvement in battery performance as well as the development of behind-the-meter and in-front of the meter storage opportunities in the future, the storage capacity of batteries will increase significantly which makes the quality, reliability and life (QRL) of batteries immensely more important than ever before, therefore an effective battery sensing system is of crucial need.

Traditional batteries are passive sources of energy and power where there is no direct control of the electrical output. A conventional battery management system (BMS) monitors the functional status of batteries (terminal voltage, current and pack temperature) to further estimate State of Charge (SoC) as well as State of Health (SoH) and ultimately manages the batteries during cycling. However, due to relatively few monitored parameters and limited understanding of cell operation have led batteries to still face some technological challenges of accurately predicting the states and controlling the operation, which seriously influence the QRL of the batteries. An effective battery sensing system with high performance and easy implementation is expected to address the challenges. Nascimento et al. [5] embedded a hybrid sensing network into a Li-ion battery pouch cell to monitor and simultaneously discriminate the internal strain and temperature variations in real time,

* Corresponding author.
E-mail address: yifei.yu.1@warwick.ac.uk (Y. Yu).

https://doi.org/10.1016/j.rser.2021.111514
Received 22 November 2020; Received in revised form 7 July 2021; Accepted 16 July 2021
Available online 21 July 2021

Abbreviations

AGFFPI	Air-Gap Fibre Fabry–Perot Interferometer
BMS	Battery Management System
CAN	Controller Area Network
CE	Counter Electrode
CIR	Circulator
C-OFDR	Coherent Optical Frequency Domain Reflectometry
DAQ	Data Acquisition card
DOFS	Distributed Optical Fibre Sensor
ECM	Equivalent Circuit Model
EIS	Electrochemical Impedance Spectroscope
EM	Electron Microscopy
EV	Electric Vehicle
FBG	Fibre Bragg Grating
FPI	Fabry-Perot Interferometer
FUT	Fibre Under Test
HEV	Hybrid Electric Vehicle
LED	Light Emitting Diode
LSPR	Localized Surface Plasmon Resonance
MMF	Multimode Fibre
MZI	Mach-Zehnder Interferometer
OC	Optical Coupler
OFS	Optical Fibre Sensor
PBS	Polarisation Beam Splitter
PC	Polarisation Controller
PCF	Photonic Crystal Fibre
PD	Photo Detector
PMMA	Poly Methyl Methacrylate Acid
PtTFPP	Platinum Tetrakis Pentafluorophenyl Porphine
QRL	Quality, Reliability and Life
RBS	Rayleigh Backscattered Spectrum
RE	Reference Electrode
RH	Relative Humidity
RI	Refractive Index
RTD	Resistance Temperature Detector
SEI	Solid Electrolyte Interface
SMF	Single Mode Fibre
SoC	State of Charge
SoH	State of Health
SoP	State of Power
SPI	Serial Peripheral Interface
SPR	Surface Plasmon Resonance
SRI	Surrounding Refractive Index
STEM	Scanning Transmission Electron Microscope
TC	Thermocouple
TCF	Thin-Core Fibre
TFBG	Tilted Fibre Bragg Grating
TLS	Tunable Laser Source
TOF	Tapered Optical Fibre
VRFB	all-Vanadium Redox Flow Battery
WE	Working Electrode
XRD	X-ray Diffraction
XPS	X-ray Photoelectron Spectroscopy

Symbol	*Description*	*Unit*
A	Constant coefficient	
C	Residual discharge capacity or Concentration	Ah *or* w/w
c	Speed of light in space	m/s
d	Distance	m
d_p	Penetration depth	m
E	Electrical field of light or Young's modulus	V *or* Pa
ΔF	Frequency tuning range of TLS	Hz
f_B	Beat frequency	Hz
h	Planck constant	$J{\cdot}s$
I	Light intensity	W
K_T	Temperature sensitivity	m/K *or* Hz/K
K_ε	Strain sensitivity	m *or* Hz
k	Integer or Rate or Propagation constant	$-$ *or* $-$ $orrad/m$
L *orl*	Length	m
m	Sensitivity of $\Delta\lambda$	m
n	RI	
Δn	RI variation	
$[O_2]$	Oxygen concentration	g/m^3
P	Strain-optical coefficient	
p_e	Photoelastic constant of fibre	
S	Energy singlet state	J
T	Temperature or Energy triplet state	K *or* J
ΔT	Temperature variation	K
t	Time	s
V	Volume	L
z	Position along the FUT	m
Δz	Spatial resolution	m
α	Thermal expansion coefficient of fibre	K^{-1}
σ	Stress	Pa
θ	Angle	∘
ε	Temperature correlated absorption coefficient	
φ	Quantum efficiency	
τ	Fluorescence lifetime	s
ε	Strain or Dielectric constant $-$ *or* $-$	
$\Delta\varepsilon$	Strain variation	
δ_{FPI}	Phase difference	
ξ	Thermo-optic coefficient of fibre	K^{-1}
Λ	Grating period	m
λ	Wavelength	m
$\Delta\lambda$	Wavelength shift	m
ω	Angular frequency	rad/s
ν	Poisson's ratio or Frequency $-$	*or* Hz
$\Delta\nu$	Frequency shift	Hz

the results directly gave more accurate information for states estimation which is crucial for a safe and reliable operation. Moreover, the sensing dataset provided the details of heat and stress evolution in the batteries that can help scientists and engineers deepen their understanding of the internal structure and the underpinning the creation of new mathematical models of the battery. This will in turn further help in the development of battery chemistry and optimise future battery design. In addition, battery sensing can present evidences of early indication of performance degradation.

Over the years, various battery sensing methods have been demonstrated to examine different battery chemistries, Dominko et al. [6] gave a statistical result of the available sensing technologies proposed in patents for battery modules and systems. So far, it concluded that optical fibre sensors (fibre Bragg grating, evanescent wave spectroscopy and other fibre optics) accounted for the highest proportion. To further investigate the academic tendency of battery sensing methods, the last 5 years' research articles have been reviewed and catalogued, as shown in Fig. 1 wherein the methods for current/voltage sensing are not included due to their mature development. The results straightforward show that optical fibre sensing methods (marked with red shadow) are predominantly attracting increased interest compared to other sensing methods. Table 1 lists some of the main sensing methods being developed for monitoring different parameters: temperature, strain and SoC/SoH.

Temperature is an essential factor to determine the safe and reliable

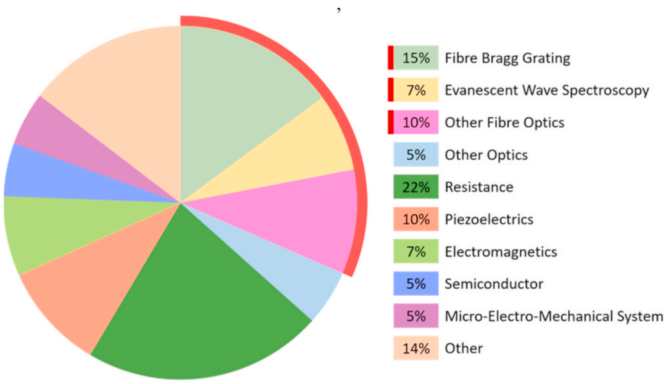

Fig. 1. Available sensing methods for battery.

Table 1
Various battery sensing methods.

Parameter	Method	Implementation	Destructiveness	Ref.
Temperature	Thermocouple (TC)	Internal & External	Non-destructive	[8, 9]
Temperature	Thermistor	Internal & External	Non-destructive	[10, 11]
Temperature	Resistance Temperature Detector (RTD)	Internal & External	Non-destructive	[12, 13]
Temperature	Thermographic Imaging	External	Non-destructive	[14]
Temperature	Infrared Thermal Imaging	External	Non-destructive	[15]
Strain	Strain-gauge	External	Non-destructive	[17]
Strain	Load Cell	External	Non-destructive	[18]
Strain	Digital Image Correlation	External	Non-destructive	[19]
Strain	X-ray Photoelectron Spectroscopy (XPS)	External	Destructive	[20]
Strain	X-ray Diffraction (XRD)	External	Destructive	[21]
SoC/SoH	Electrochemical Impedance Spectroscope (EIS)	External	Non-destructive	[24]
SoC/SoH	Equivalent Circuit Model (ECM)	External	Non-destructive	[26]
SoC/SoH	Machine Learning Algorithm	External	Non-destructive	[27]
SoC/SoH	Electron Microscopy (EM)	External	Destructive	[30]
SoC/SoH	Scanning Transmission Electron Microscope (STEM)	External	Destructive	[31]
Temperature & Strain & SoC/SoH	Optical Fibre Sensor	Internal & External	Non-destructive	[32, 33]

operation of batteries due to temperature gradients which can lead to local ageing differences and hence to global ageing of batteries. Moreover, failures, thermal runaway, venting, fire and explosion of batteries could occur under insufficient cooling or abusive conditions [7], thus it has called for numerous temperature sensing methods for batteries. The well-known traditional methods such as thermocouple (TC) [8,9], thermistor [10,11] and resistance temperature detector (RTD) [12,13] are commonly applied to monitor the surface temperature in general deployments, while TC and RTD are more widely used to measure the internal temperature in a lab. They have the advantages of high sensitivity, small size, fast response time and low cost, however, their challenges include residing in the positioning and wiring without affecting the performance of batteries. In addition, these methods, as single point measurement technologies, are inadequate to obtain the spatially non-uniform temperature distribution, thus thermographic imaging [14] and infrared thermal imaging [15] are two popular methods to observe the surface temperature distribution and the hot spots within the cell with complex configuration, poor spatial resolution and limited temperature accuracy. Since the surface temperature is significantly lower than the actual maximum temperature of batteries [7], monitoring of the internal temperature is more helpful and more accurate to keep the batteries operating in the optimal working temperature range and to improve the QRL of the batteries.

Strain is of equal importance with temperature for battery monitoring, it has resulted from the inhomogeneous electrode stress accumulation which reduces capacity and power of batteries [16]. The electrode stress can be commonly reflected either by the dimensional change or by the surface pressure of the electrode and/or a whole battery. Strain-gauge [17] is the simplest method to measure the strain by probing the total volume change of batteries. Another strain measurement method is load cell [18], it employs a constraint fixture, consisting of an amplified load cell in series with a battery cell, applied with an initial load to monitor the stack level mechanical stress in real-time. Digital image correlation [19] is a non-contact optical technique which directly measures the strain, in two or three dimensions, by tracking a unique pattern on the surface through a sequence of digital images. X-ray photoelectron spectroscopy (XPS) [20] and X-ray diffraction (XRD) [21] are two destructive methods to directly measure the strain inside the battery instead of monitoring the cell volume variation externally.

SoC is a critical parameter which indicates the current and remaining performance of the battery [22]. On the other hand, SoH is an important indicator of the battery's life and ability to deliver or receive energy [23]. However, neither SoC nor SoH can be observed directly because of the non-linear, time-varying characteristics and electrochemical reactions. Therefore, estimation of SoC/SoH relies on a combination of the physical properties of batteries and various models and algorithms. A wide variety of estimation methods have been developed over the years, in which electrochemical impedance spectroscope (EIS) [24] is a conventional method to decipher the electrochemical processes that are closely related to battery impedance [25], it has been implemented to estimate SoC/SoH of batteries and to develop various equivalent circuit models (ECMs) [26] which also are used to estimate the SoC/SoH underpinning the design of adaptive filter algorithms and non-linear observers, for example different derivatives of the Kalman Filter implementation. Machine learning algorithms [27] are exploited to accurately predict SoC/SoH of batteries even to quantify the SoC/SoH variability among cells in battery packs [28,29] owing to their strong capability of data processing and nonlinear fitting. Furthermore, both electron microscopy (EM) [30] and scanning transmission electron microscope (STEM) [31] are employed to estimate SoC/SoH of batteries by characterizing the detailed evolution of the Li electrodeposition and the solid electrolyte interface (SEI) layer at the atomic scale in a destructive way.

Among all the battery sensing methods, optical fibre sensor (OFS) [32,33] is an emerging technology which can be attached to the surface as well as embedded inside the battery to measure the temperature, strain and other parameters in real-time, to estimate SoC/SoH with the help of algorithms. As highlighted within [34], accurately sensing with fine temporal and spatial resolution is essential for an advanced and intelligent battery to ensure safe and reliable operation, estimate and predict the real-time states and provide a basis for thermal management, power management as well as life management of batteries.

To the best of our knowledge, there is no such review on optical fibre sensing methods for batteries, the present review therefore contributes to close this knowledge gap by discussing the current developments in

optical fibre sensing methods for batteries. Various optical fibre sensing methods applied to batteries are reviewed and discussed systematically in terms of the working principles. Followed by an overview of the sensing performance corresponding to different sensing parameters. Challenges and outlooks are revealed before a conclusion is made at the end of the present review.

The remainder of this review is organized as follows: Section 2 discusses the working principles relying on the following categories: optical fibre grating sensors, optical fibre interferometer sensors, optical fibre evanescent wave sensors, optical fibre photoluminescent sensors and optical fibre scattering sensors. Section 3 reviews the sensing performance with the methods discussed above. Section 4 lists the current challenges and gives the outlooks for future research, and finally, Section 5 summarizes the paper.

2. Optical fibre sensing methods for batteries

The purpose of battery sensing is to assist the BMS to control the flow of energy to and from the battery, as well as to ensure the safe and optimal use of the energy inside the battery. Among all the sensing methods adopted in batteries, the ones that can measure multiple parameters at various locations both inside and outside the batteries in real-time are of prime importance. The optical fibre sensing methods are expected to be one of the most promising sensing methods for batteries in the future due to their capability of acquiring multiple parameters with high speed and sensitivity [5], being able to be composited in multiplexed configurations [32,35], working without interfering the battery performance [36,37] and being robust to various harsh environment conditions [38]. There are five representative types of optical fibre sensing methods for batteries, called optical fibre grating [39], optical fibre interferometer [5], optical fibre evanescent wave [40], optical fibre photoluminescent [41] and optical fibre scattering [42]. The operating principles for each type of methods are presented.

2.1. Optical fibre grating sensors

2.1.1. Fibre Bragg Grating

Optical Fibre Bragg Grating (FBG) sensors are extensively investigated and used in measuring local static and fluctuating temperature, strain, bending, pressure and refractive index (RI) in electrochemical systems such as polymer electrolyte membrane fuel cells [43–47] and Li-ion batteries [48–52].

An FBG sensor typically consists of a short segment of a single-mode optical fibre with a photoinduced periodically modulated RI in the core of the fibre. The length of an FBG sensor is usually a few millimetres. When the FBG sensor is illuminated with a broadband optical signal, as shown in Fig. 2(a), the wavelength of the reflected signal can be given as

$$\lambda_B = 2n_{eff}\Lambda \tag{1}$$

where Λ is the grating period, n_{eff} is the effective RI of the fibre core, λ_B is the so-called Bragg wavelength.

When the FBG sensor is exposed to external influences, take temperature T (Fig. 2(b)) and strain ε (Fig. 2(c)) as examples, the response to the temperature variation ΔT and the strain variation $\Delta\varepsilon$ can be determined by

$$\Delta\lambda_B = \lambda_B\left(\frac{1}{n_{eff}}\frac{\partial n_{eff}}{\partial T}+\frac{1}{\Lambda}\frac{\partial\Lambda}{\partial T}\right)\Delta T = \lambda_B\Big(\alpha+\xi\Big)\Delta T = K_T\Delta T \tag{2}$$

$$\Delta\lambda_B = \lambda_B\left(\frac{1}{n_{eff}}\frac{\partial n_{eff}}{\partial \varepsilon}+\frac{1}{\Lambda}\frac{\partial\Lambda}{\partial \varepsilon}\right)\Delta\varepsilon = \lambda_B\Big(1-p_e\Big)\Delta\varepsilon = K_\varepsilon\Delta\varepsilon \tag{3}$$

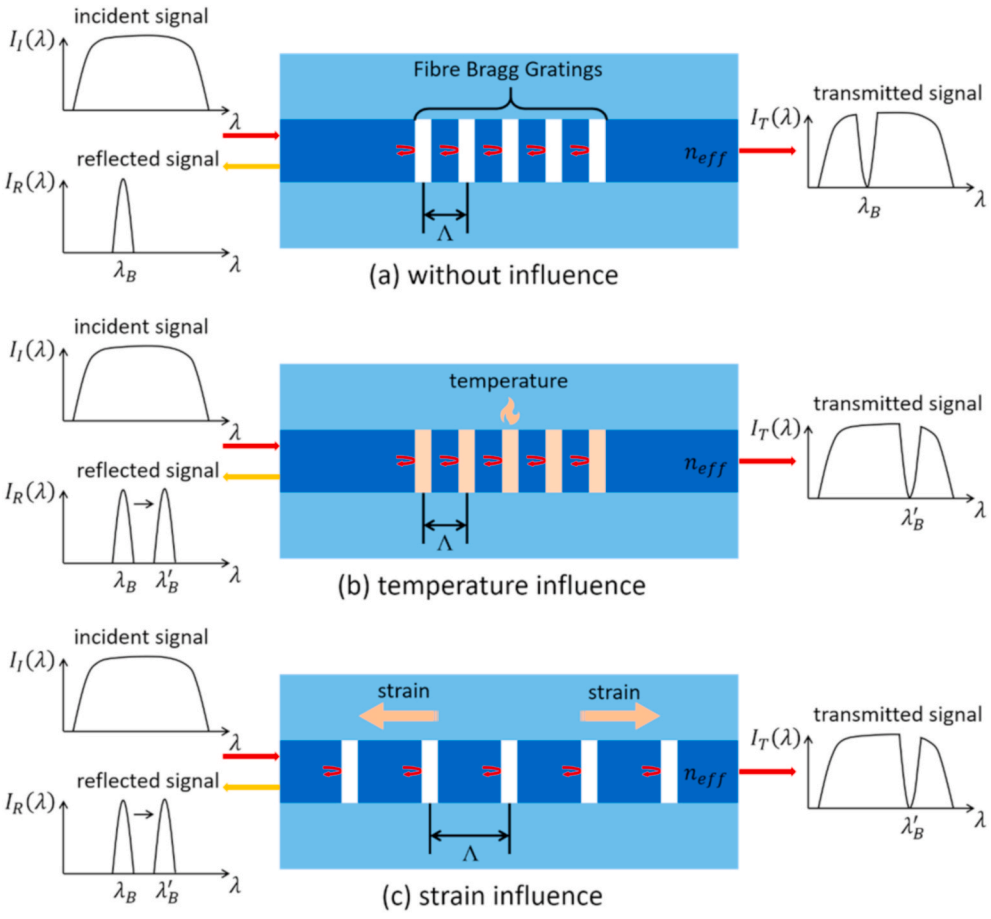

Fig. 2. Typical scheme and operating mechanism of an FBG sensor. I_I stands for the incident broadband optical signal, I_R and I_T stand for the reflected and transmitted signals, respectively. (a) without influence, when the FBG sensor is illuminated with a broadband optical signal, a specific wavelength is reflected with a sharp peak power spectrum, while the transmitted signal remains nearly unaffected; when the FBG sensor is exposed to (b) temperature influence or/and (c) strain influence, a shift in the Bragg wavelength presents due to the changes in n_{eff} and Λ caused by the external variations.

where $\Delta\lambda_B$ is the shift in the Bragg wavelength, α and ξ are the thermal expansion and thermo-optic coefficients of the optical fibre material, respectively. p_e is the photoelastic constant of the fibre, K_T and K_ε are the temperature and strain sensitivities, respectively.

2.1.2. Tilted Fibre Bragg Grating

Compared to the conventional FBG sensors discussed above, Tilted Fibre Bragg Grating (TFBG) sensors have a special configuration which leads to the enhanced sensitivity to the surrounding refractive index (SRI). Thus, the TFBG sensors have been advantageously employed in sensing temperature [53], liquid level [54], SRI [55], relative humidity (RH) [56] and pH [57] in the chemical and biochemical areas. Among the applications, Lao et al. [33] adopted a TFBG sensor to detect the SoC of supercapacitors.

In a typical TFBG sensor, as shown in Fig. 3, the tilt angle θ gives rise to an effective coupling of part of the transmitted core mode to the co-propagating or counter-propagating cladding modes depending on θ. The wavelength of the coupled i -th cladding mode $\lambda_{cl(i)}$ can be expressed as

$$\lambda_{cl}\left(i\right) = \left(n_{eff}^{core} + n_{eff}^{cl}\left(i\right)\right)\Lambda = \frac{\left(n_{eff}^{core} + n_{eff}^{cl}\left(i\right)\right)\Lambda_g}{\cos\theta} \tag{4}$$

where n_{eff}^{core} and $n_{eff(i)}^{cl}$ are the effective RIs of the fibre core and the i -th cladding mode, respectively. Λ and Λ_g are the grating periods along the fibre longitudinal axis and perpendicular to the grating plane, respectively.

The excited cladding modes are confined in the fibre cladding by total internal reflection on the cladding-surrounding medium interface. Each of the cladding modes propagates with a corresponding effective RI value. When the RI value of the surrounding medium reaches the one of a specific cladding mode, the cladding mode will be coupled out of the fibre cladding, resulting in a change in the grating transmission spectrum. Therefore, the variations of the SRI can be quantitatively detected by monitoring the changes in the grating transmission spectrum of the TFBG.

2.2. Optical fibre interferometer sensors

2.2.1. Mach-Zehnder Interferometer

Mach-Zehnder Interferometer (MZI) sensors (or fibre modal interferometer sensors) are widely adopted for sensing temperature [58], strain [59], curvature [60], SRI [61], liquid level [62], RH [63], pH [64] and so on because of its advantages of high RI sensitivity and flexible configurations, as shown in Fig. 4.

An MZI is formed due to the phase difference between the fundamental core mode and the higher order cladding modes in fibre. Consequently, peaks or dips in the interference spectrum are formed. For simplicity, only the core mode (I_1) and one cladding mode (I_2) are taken into consideration. The transmitted interference signal I can be expressed as

$$I = I_1 + I_2 + 2\sqrt{I_1 I_2}\cos\left[\frac{2\pi\left(n_{eff}^{core} - n_{eff}^{cl}\right)L}{\lambda_I}\right] \tag{5}$$

It reaches a minimum $I = I_{min}$ when the interferometric phase difference satisfies the following condition

$$\frac{2\pi\left(n_{eff}^{core} - n_{eff}^{cl}\right)L}{\lambda_\nu} = \left(2k+1\right)\pi \tag{6}$$

where n_{eff}^{core} and n_{eff}^{cl} are the effective RIs of the fibre core and cladding mode, respectively. λ_I is the input optical wavelength, L is the interferometric length, k is an integer ($k = 0, 1, 2, \ldots$) and λ_ν is the central wavelength of the interference valley of the k -th order that can be expressed as

$$\lambda_\nu = \frac{2\left(n_{eff}^{core} - n_{eff}^{cl}\right)L}{2k+1} \tag{7}$$

When a change of the surrounding environment occurs, the difference of the effective RI will vary by $\Delta n_{eff} = \Delta n_{eff}^{core} - \Delta n_{eff}^{cl} \approx \Delta n_{eff}^{cl}$, finally λ_ν will have a shift of

$$\Delta\lambda_\nu = \frac{2\Delta n_{eff} L}{2k+1} \approx \frac{2\Delta n_{eff}^{cl} L}{2k+1} \tag{8}$$

Therefore, the variations of the surrounding environment can be detected by tracking the wavelength shifts of the interference spectrum.

2.2.2. Fabry-Perot Interferometer

Fabry-Perot Interferometer (FPI) sensors, a type of optical fibre interferometer sensor, are proposed to monitor strain or pressure variations due to their high strain sensitivity [65] and utilised for measurement of RI [66,67], temperature [68], gas pressure [69], RH [70], Carbon dioxide [71], magnetic field [72], ultrasound [73] and microfluidic velocity [74]. Recent study shows that they are becoming the popular candidates to improve the discrimination of strain and temperature in batteries [5].

Although various shaped FPI sensor cavities are designed, such as rectangular [75], spheroidal [76], hollow tube [77] and crescent [65], a simplest FPI sensor is composed with a cavity which has two parallel reflecting surfaces separated by a certain distance, as shown in Fig. 5(a), due to the optical phase difference between two reflected signals, the reflection spectrum of an FPI can be described as the wavelength dependent intensity modulation of the incident signal spectrum. The phase difference of the FPI (δ_{FPI}) can be given as

$$\delta_{FPI} = \frac{4\pi nL}{\lambda} \tag{9}$$

where n is the RI of the cavity material, L is the physical length of the cavity and λ is the wavelength of the output signal.

Thus, an introduced perturbation to the FPI sensor, take a longitudinal strain (Fig. 5(b)) as example, can be obtained by measuring the wavelength shift of the spectrum of an FPI sensor.

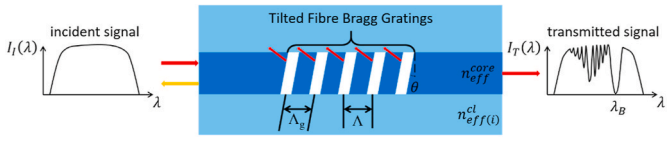

Fig. 3. Typical scheme of a TFBG sensor. The periodic modulation pattern of the RI of the fibre core is uniformly tilted by an angle θ perpendicular to the fibre longitudinal axis. I_I and I_T stand for the incident broadband optical signal and the transmitted signal, respectively. The excited discrete cladding modes appear on the grating transmission spectrum as a series of narrow attenuation peaks which generally locate in the shorter wavelength range of the main attenuation band.

2.3. Optical fibre evanescent wave sensors

Optical fibre evanescent wave sensors are based on the interaction of the evanescent field in the cladding with the fibre's surroundings, resulting in changes of the transmitted spectrum. It follows that they possess the capability of translating a change of the target analyte into optical signals so that they are widely applied to chemical sensing [78]

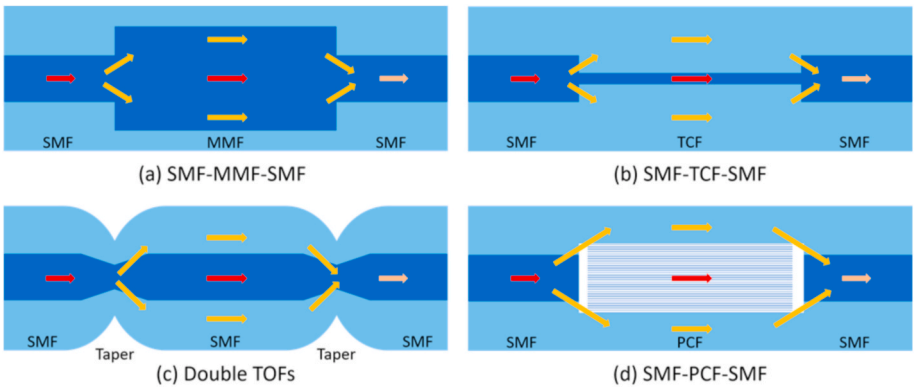

Fig. 4. Several configurations of MZI sensors. The methods implemented include combining (a) multimode fibre (MMF) [58]; (b) thin-core fibre (TCF) [59]; (c) tapered optical fibre (TOF) [61]; (d) photonic crystal fibre (PCF) [63] with single mode fibre (SMF) in a hybrid structure.

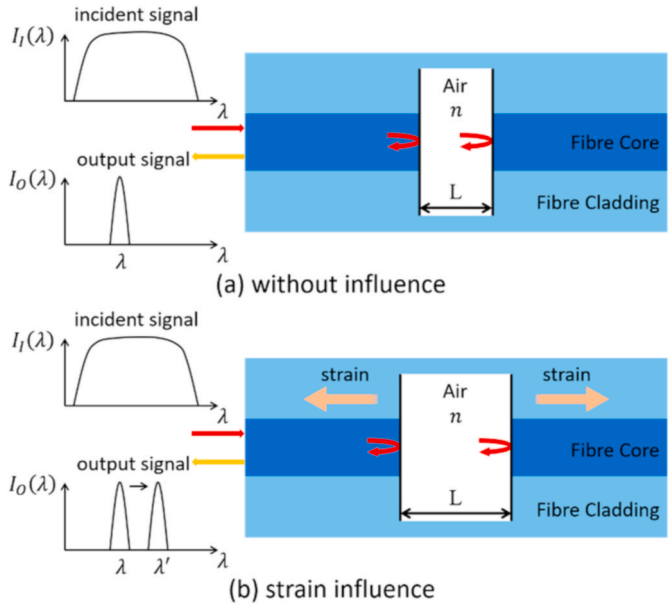

Fig. 5. Operating mechanism of an FPI sensor. (a) without influence, when the incident signal (I_I) transmitting along the fibre core, it will be reflected by the two surfaces of the FP cavity respectively, the output signal (I_O) is an interference signal resulted from the multiple superpositions of both reflected and transmitted signals; (b) strain influence, when inducing a longitudinal strain perturbation to the FPI sensor, a change of the phase difference of the FPI occurs because of the variation in the optical path difference of the interferometer resulted from the variation of L or/and n.

and biosensing [79]. In 2018, Lao et al. [33] demonstrated a surface plasmon resonance (SPR)-based optical fibre sensor to monitor the electrochemical activity in supercapacitors for the first time.

As shown in Fig. 6, the evanescent field $E_{ew}(d)$ decays exponentially as

$$E_{ew}(d) = E_0 exp(\frac{-d}{d_p}) \tag{10}$$

where E_0 is the magnitude of the field at the fibre core-cladding interface, d is the distance from the core-cladding interface, d_p is the distance where the evanescent field decreases to E_0/e and is described as the penetration depth which is given by

$$d_p = \frac{\lambda}{2\pi\sqrt{n_{co}^2 \sin^2\theta - n_{cl}^2}} \tag{11}$$

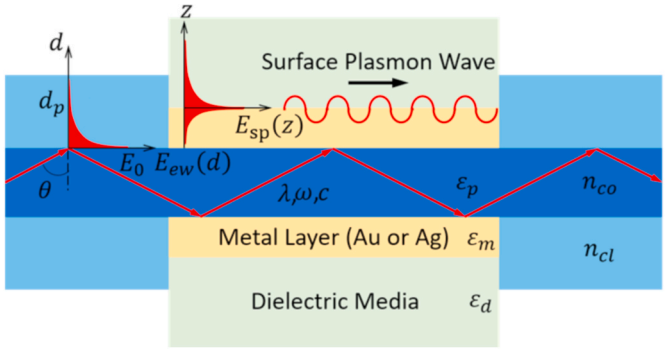

Fig. 6. Illustrations of evanescent field and surface plasmon resonance. $E_{ew}(d)$ and $E_{sp}(z)$ refer to evanescent field and surface plasmon resonance, respectively. z is the distance from the metal-dielectric interface.

where λ is the wavelength of the incident light, θ is the angle of incidence at the fibre core-cladding interface, n_{co} and n_{cl} are the RIs of the fibre core and cladding, respectively.

The SPR is a collective oscillation of free electrons excited by light at the metal-dielectric interface. The electromagnetic field decays exponentially into both the metal and the dielectric, the propagation constant of the SPR can be given as

$$k_{sp} = \frac{\omega}{c}\sqrt{\frac{\varepsilon_m \varepsilon_d}{\varepsilon_m + \varepsilon_d}} \tag{12}$$

and the propagation constant of the evanescent wave parallel to the planar metal film surface can be expressed as

$$k_{ew} = \frac{\omega}{c}\sqrt{\varepsilon_p}\sin\theta \tag{13}$$

where ω is the angular frequency of the incident light, c is the speed of light in space. ε_m, ε_d and ε_p are the dielectric constants of the metal, dielectric and optical fibre, respectively.

The SPR occurs when $k_{sp} = k_{ew}$, it exhibits high sensitivity to even slight fluctuations in the dielectric constant of the dielectric. Consequently, SPR-based sensors can effectively detect distinct variables due to the position of the resonance (incident wavelength or angle) shifts with the varying of the RI of the surrounding dielectric.

In addition, the increase in the evanescent field results in the enhancement of the sensing sensitivity and selectivity. Apart from the penetration depth, the evanescent field also increases due to the coupling of modes in a multimode fibre. Fig. 7 illustrates the profiles of the sensing fibres. However, the penetration depth is still small, different additional transduction mechanisms such as refractive index induced

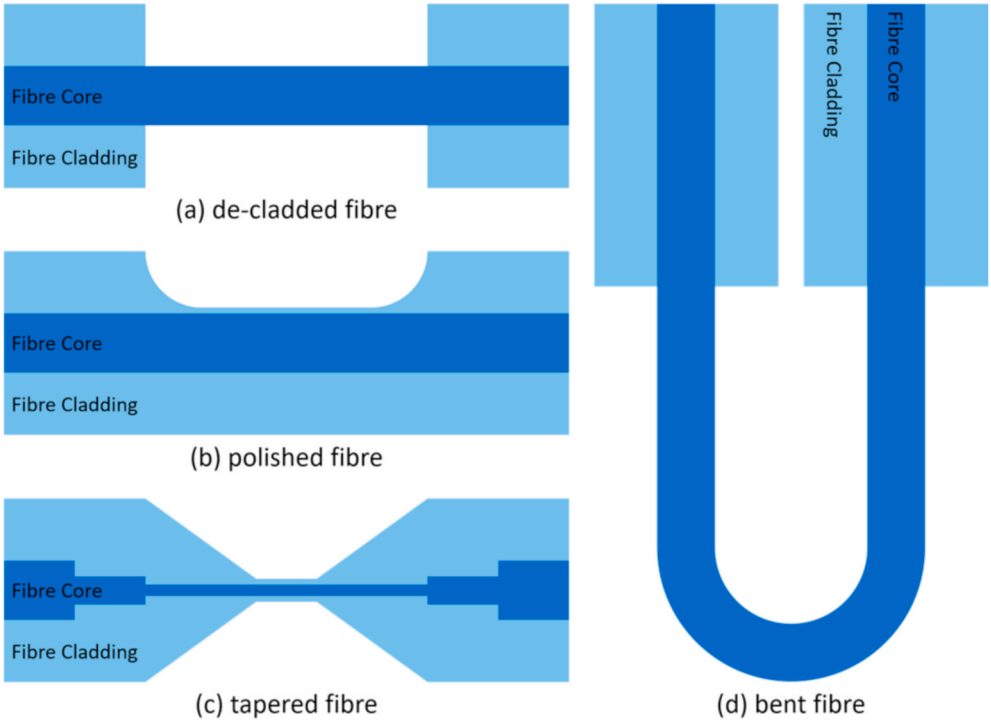

Fig. 7. Several fibre geometries. They are based on (a) de-cladding [80], (b) polishing [81], (c) tapering [82] and (d) bending [83] to achieve the evanescent wave sensors as well as the increase in the penetration depth and facilitate the mode coupling.

intensity change [84], evanescent field absorption [85], evanescent field fluorescence [86] and SPR [87] have been investigated to amplify the response signal.

2.4. Optical fibre photoluminescent sensors

Optical fibre fluorescent sensors, a type of optical fibre photoluminescent sensor, are maturely developed and employed to monitor the internal temperature of batteries [41,86]. Recently, optical fibre phosphorescent sensors are adopted to measure the oxygen concentration in the porous cathode of a lithium–air battery [88].

The working principle is primarily based on photoluminescence, as shown in Fig. 8. For a fluorescent substance of a given concentration C and volume V, the intensity of the fluorescence I_f can be expressed as

$$I_f = I_{in} C V \varepsilon \varphi \tag{14}$$

where I_{in} is the intensity of the incident light, ε is the temperature correlated absorption coefficient and φ is the quantum efficiency of fluorescence which is strongly dependent on temperature. The modulation of I_f as a single-valued function of temperature forms the fundamental principle of the fluorescence intensity measurement method [86].

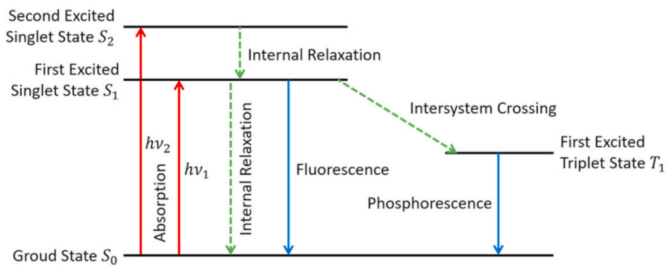

Fig. 8. Illustration of photoluminescence. When the electrons in the luminescent substance are excited by the excitation light, the electrons absorb the energy from the photons ($h\nu_1$ or $h\nu_2$) and transition from S_0 to S_1 or S_2, then the electrons in S_2 move to S_1 via internal relaxation due to the instability of S_2. As a result, a fraction of the electrons in S_1 moves to T_1 via intersystem crossing and finally generates the phosphorescence, another fraction of the electrons returns to S_0 along with the emission of the fluorescence. Meanwhile, other electrons reach to S_0 via non-radiative internal relaxation.

When the excitation light fades, I_f single-exponentially decays as

$$I_f(t) = A I_f(t_0) e^{-\frac{t}{\tau}} \tag{15}$$

where A is a constant coefficient, $I_f(t_0)$ is the intensity of the fluorescence when the excitation light stops, τ is the fluorescence lifetime which has a single function relationship with temperature. Furthermore, τ is not affected by the fluctuations in light intensity. Thus, temperature can be monitored by measuring τ. This is how the fluorescence lifetime measurement method works [41].

2.5. Optical fibre scattering sensors

Distributed Optical Fibre Sensors (DOFSs), also known as optical fibre scattering sensors, are based on the Rayleigh [89], Brillouin [90] and Raman [91] scattering effects in optical fibres. DOFSs have found wide applications such as structural health monitoring of civil engineering structures [92], geohazards prevention [93], health and safety monitoring of composite materials [94] and quantitative chemical monitoring [95]. In a recent study [42]., the Coherent Optical Frequency Domain Reflectometry (C-OFDR), a type of Rayleigh scattering based DOFS, is performed to monitor Li-ion batteries due to its high spatial resolution and simple configuration compared to other DOFSs.

A typical configuration of C-OFDR is illustrated in Fig. 9. By analysing the interference signal of the main interferometer, it can be found that a specific beat frequency f_B directly corresponds to a specific position z along the FUT. The spatial resolution Δz can be given as

$$\Delta z = \frac{c}{2 n_g \Delta F} \tag{16}$$

where c is the speed of light in space, n_g is the group RI and ΔF is the

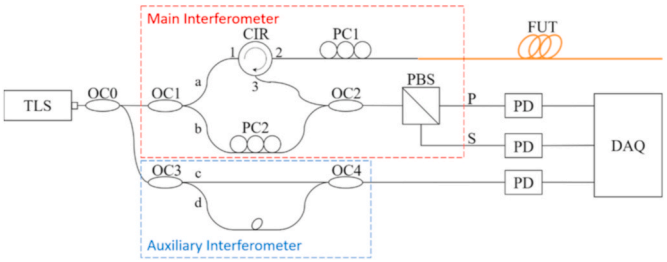

Fig. 9. Typical configuration of a C-OFDR. It consists of a main interferometer and an auxiliary interferometer. The main interferometer contains two optical couplers (OC1 and OC2), an optical circulator (CIR), two polarisation controllers (PC1 and PC2), a fibre under test (FUT) and a polarisation beam splitter (PBS). The auxiliary interferometer includes two optical couplers (OC3 and OC4). The optical frequency of the output laser from the tunable laser source (TLS) is linearly tuned in time, the laser splits into two arms after undergoing the OC0. Then the frequency tuning laser launched into the main interferometer splits into two portions at the OC1: one (light a) enters the CIR, the PC1 and the FUT, the other (light b) enters the PC2. The spontaneous Rayleigh backscattering light in the FUT interferes with light b at the OC2. The interference light launches into the PBS and then splits into two orthogonal polarisation components (P and S). P and S are detected by the photo detectors (PDs) and stored by the data acquisition card (DAQ). Meanwhile, the laser launched into the auxiliary interferometer splits into light c and light d, an interference between them occurs at the OC4, the interference light is employed as a trigger signal to mitigate the tuning nonlinearity.

frequency tuning range of the TLS.

In known conditions, a stable and unique fingerprint Rayleigh backscattered spectrum (RBS) is acquired. The local RBS shifts when an environment variation occurs. The cross-correlation of the measurement RBS and the fingerprint RBS determines the local spectral shift $\Delta\nu$, which can reveal local information (temperature, strain and vibration) along the whole fibre by using proper calibration constants. Assuming the temperature and strain responses are essentially independent, then the relationship between $\Delta\nu$ and the temperature variation ΔT and the strain variation $\Delta\varepsilon$ can be described as

$$\Delta\nu = K_T\Delta T + K_\varepsilon\Delta\varepsilon \tag{17}$$

where K_T and K_ε are the temperature and strain sensitivities, respectively.

3. Battery sensing based on optical fibre sensors

The methods discussed above have been conjunctively applied to the battery sensing, in the aspects of measuring temperature, strain (stress), RI, electrolyte density, flow change, oxygen concentration, SoC and SoH, the sensing parameters corresponding to each method are presented in Fig. 10.

3.1. Temperature measurement

Both the surface and internal temperature variations of Li-ion batteries, demonstrated by pouch cell and cylindrical cell, are monitored by the optical fibre sensing technologies both in-situ and in-operando. The applied methods mainly focus on the FBG sensors, then the photoluminescent sensors combined with the evanescent wave sensors, besides, the scattering sensors are new employers in battery sensing area. The results are introduced by publication time based on different research groups.

Du et al. [41] invented a measuring device for monitoring the internal temperature of a Li-ion battery in 2011. The schematic of the proposed device is illustrated in Fig. 11, where the light emitting diode (LED) at 470 nm worked as the excitation light source driven by an

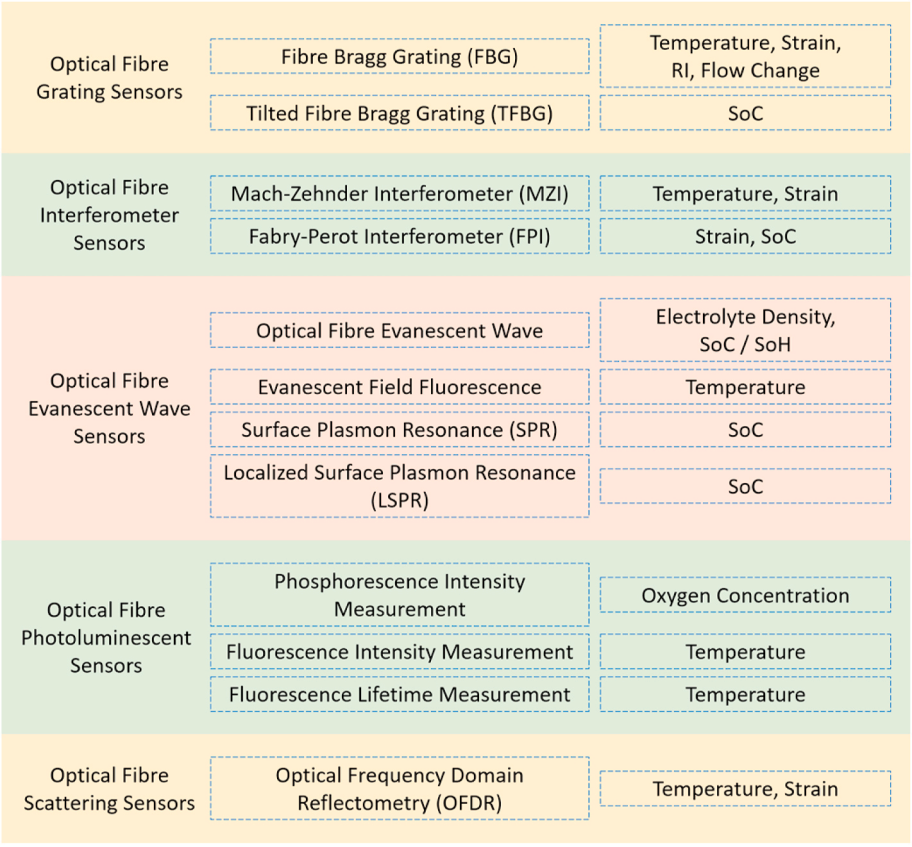

Fig. 10. Various optical fibre sensing methods for batteries.

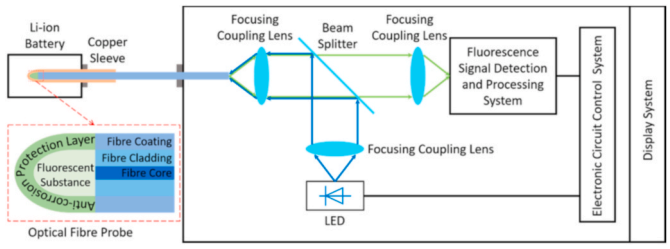

Fig. 11. Schematic of a device based on fluorescence lifetime measurement method. Adapted from Ref. [41]. Copyright 2011.

electronic circuit control system; the optical coupling system consisted of three focusing coupling lenses and a beam splitter that reflected the light at 470 nm and transmit the light near 510 nm; a nickel-coated corrosion-resistant fluorescent fibre was adopted as the optical fibre probe which was embedded in a copper sleeve inside a Li-ion battery; the fluorescence signal was detected and the fluorescence lifetime was measured by a detection and processing system; the internal temperature of the battery was monitored and displayed in real time by a display system. The device was able to realise a measurement range of −50–350 °C with an accuracy higher than ±0.5 °C and directly obtain the temperature distribution inside the battery by implementing multiple optical fibre probes.

Yang et al. [48] integrated FBG sensors in Li-ion batteries to measure temperature variations in 2013 for the first time. The real-time temperature monitoring under various charge and discharge operating conditions was carried out with in situ calibration against the co-located thermocouple. A temperature resolution of 0.1 °C and a typical sensitivity of 10 p.m./°C were obtained. The experimental results showed that FBG sensors exhibit good thermal response to dynamic input and/or output of the batteries in comparison to the thermocouple.

Iyer [86] proposed a novel internal temperature measurement method based on optical fibre evanescent wave fluorescence for Li-ion battery in 2016. An etched multimode fibre coated with Poly Methyl Methacrylate Acid (PMMA) was used as the sensing region. Different from the single dye fluorescent sensor, the method adopted two different dyes, fluorescein (the donor) and Rhodamine B (the acceptor), to produce fluorescence. For an optimised sensitivity, a 0.06%*w*/*w* fluorescein as well as a 0.014% *w*/*w* Rhodamine B solution was mixed with a 5%*w*/*w* PMMA solution. The proposed temperature sensor was integrated in-line with a battery SoC sensor, as shown in Fig. 12, the active wavelength of the temperature sensor was different from the SoC sensor due to their different working principles. A y-fibre coupler was employed to couple light into the sensing fibre. An LED at 850 nm was used as the light source for real-time SoC monitoring. An LED at 470 nm was used as the fluorescent excitation light source, the intensity of the fluorescence was measured to indicate the temperature. For the multifunctional temperature and SoC sensor, the study obtained a sensitivity of 9.738 $lx/^{\circ}C$ and a resolution of 0.86 °C. However, the temperature sensor showed a theoretical resolution of 0.168 °C when solely implemented.

Nascimento et al. [39] presented an in-situ and in-operando temperature monitoring approach of Li-ion batteries in 2016. The internal

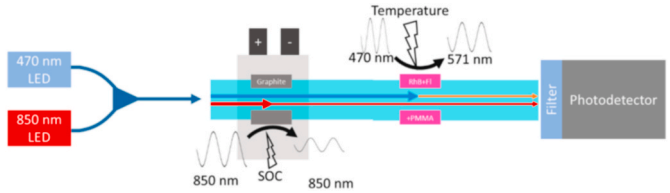

Fig. 12. Schematic of a multifunctional temperature and SoC sensor [86]. Copyright 2016.

and external temperature variations were measured by integrating two internal FBG sensors and two external FBG sensors in Li-ion pouch cells, with calibration on a thermal chamber, respectively. A smaller temperature change of 1.5 ± 0.1 °C was observed for external measurement at the centre area, while the corresponding internal temperature change was 4.0 ± 0.1 °C. The difference between the internal and external temperature changes needed to be considered for optimisation in battery modelling and BMS. The temperature variations were observed both internally and externally at different C-rates. It can be concluded that there was a direct correlation between the temperature changes and the applied current gradient. The same research group [51] conducted a comparative study between FBG sensors and K-type thermocouples (TCs) in 2017. The response rates in this study were 4.88 °C/min and 4.10 °C/min for the FBG and TC, respectively. The results showed that the FBG sensors were able to detect temperature changes with a ~1.2 times higher response rate than the K-type TCs. The rise time obtained for the FBG was 28.2 % lower than the TC, making the FBG sensors a better choice for the real-time monitoring of battery temperature. A network based on FBG sensors for monitoring surface temperature distribution on a smartphone Li-ion battery was developed by Nascimento et al. [35] in 2019. The thermal performance of five different points of a rechargeable smartphone Li-ion battery was monitored during constant current charge and different discharge rates. It was the first time to analyse the smartphone Li-ion battery thermal behaviour by taking environmental conditions, temperature and relative humidity, into account. The schematic diagram of the experimental set-up is shown in Fig. 13. The study gave a real-time thermal mapping to elucidate which areas of the battery needed to be cooled faster when it was exposed to dry, temperate and cold climates. Absolute temperature values of 30.0 ± 0.1 °C, 53.0 ± 0.1 °C and 65.0 ± 0.1 °C were achieved near the electrodes during the discharge rate of 5.77C, when exposed to the cold, temperate, and dry climates, respectively. Generally, the lower temperature variations 1.9 ± 0.1 °C were detected when the battery operated in the cold environment, while the higher temperature shifts were detected under the other two conditions, 3.5 ± 0.1 °C and 2.3 ± 0.1 °C corresponding to temperate and dry climates, respectively.

Fleming et al. [96] fabricated and demonstrated an FBG sensor to monitor the distributed temperature of a cylindrical Li-ion cell in 2018. As shown in Fig. 14(a), four 5 mm FBGs were evenly performed in an SMF-28 single-mode fibre which was threaded through a bespoke FEP coated aluminium tube and embedded within a cylindrical 18650 Li-ion cell. The fabricated FBG sensor was resistant to the strain imposed during the cell instrumentation procedure and the harsh chemical environment inside the cell. A K-type thermocouple was placed on the outside of the cell to monitor the can temperature, as illustrated in Fig. 14(b). Additionally, an environmental chamber with temperature of 25 ± 0.1 °C was employed in all the measurements. Results showed a temperature difference between the core temperature and the can

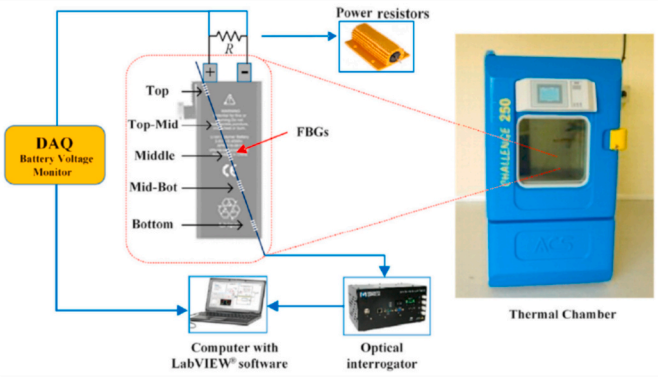

Fig. 13. Schematic of experimental set-up (left) and thermal chamber (right) [35]. Copyright 2019.

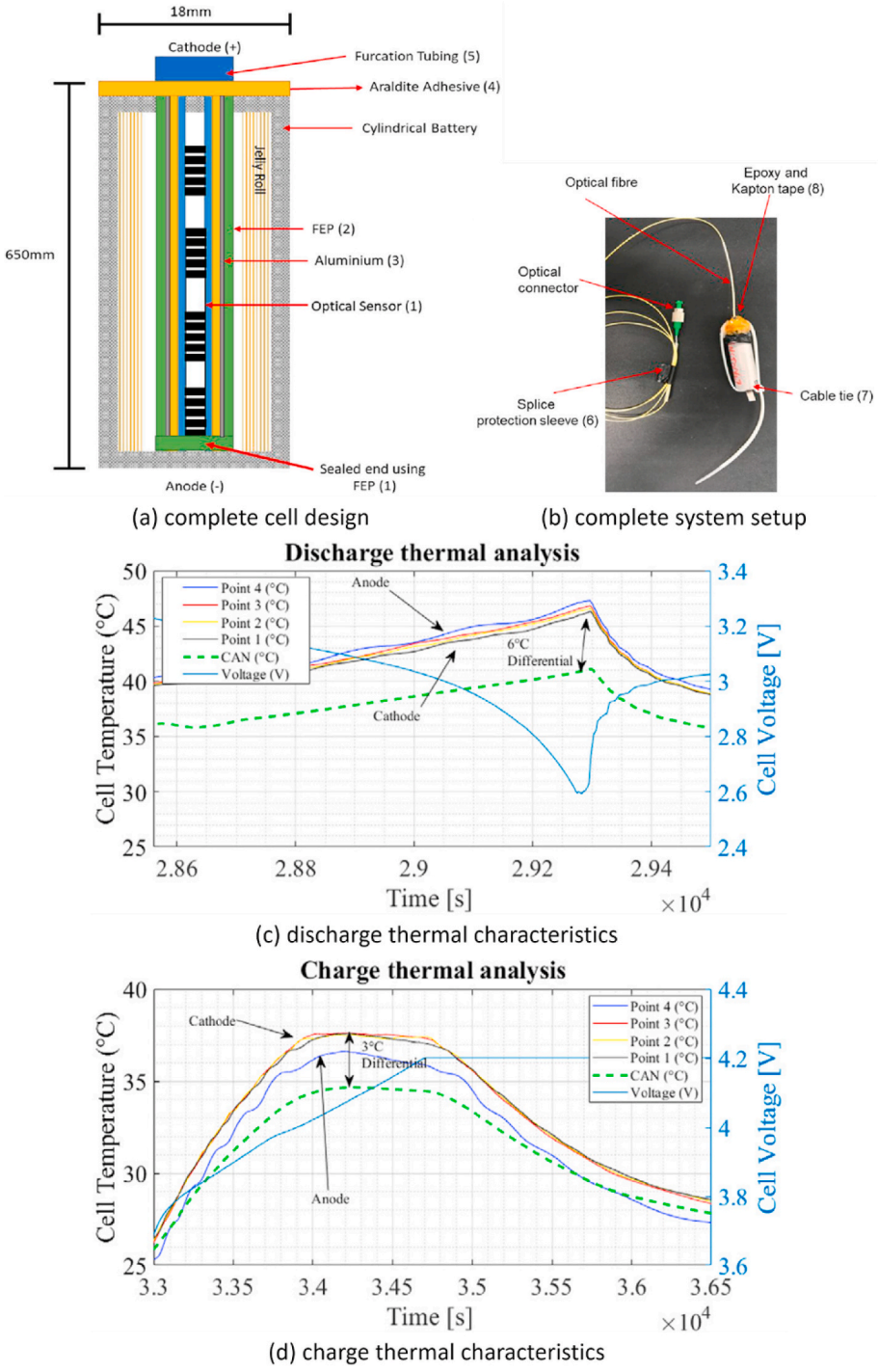

Fig. 14. FBG-based temperature measurement for cylindrical Li-ion cell. (a) complete cell design; (b) complete system setup; (c) discharge thermal characteristics; (d) charge thermal characteristics. Adapted from Ref. [96]. Copyright 2018.

temperature of up to 6 °C during the discharging process, while a temperature difference of 3 °C was obtained during the charging process, as presented in Fig. 14(c) and (d), respectively. The research also noted that the areas closer to the anode presented a higher temperature during the discharging process while the areas closer to the cathode performed a higher temperature during the charging process, meanwhile, a temperature gradient of 1 °C was observed.

Vergori et al. [97] identified the surface temperature gradients of a battery cell by using Rayleigh scattering based DOFS in 2019. The sensing fibre was put in a Polytetrafluoroethylene tube in order to remove the effect of strain. The temperature evolution over time was obtained, two TCs were attached beside the fibre. The results showed that the point sensors (TCs) had great limitations such as the necessity to have the physical space for locating, the necessity of data acquisition channels and the wires deriving from these connections. The research also tested the strain gradients with the same equipment. The study demonstrated that Rayleigh scattering based DOFS was suitable to monitor both temperature and strain gradients on Li-ion cells surface during cycling. Yu et al. [42] further investigated the thermal behaviour of a Li-ion pouch cell by deploying the C-OFDR in 2021. A 5 m long optical fibre was bonded to the surface of an A5-size pouch cell and marked as 4 regions, 8 TCs were utilised to validate the output of the

OFDR, as shown in Fig. 15(a), the experimental spatial resolution was 1.3 mm. The maximum in-plane temperature difference was measured by both TC and OFDR at different ambient temperatures during various C-rates discharge, for a 5C discharge at a 10 °C ambient temperature, a value of 11.8 °C was obtained by the OFDR while the corresponding value measured by the TC was 2.9 °C. It was highlighted by Fig. 15(b) that the OFDR results were found to be up to 307 % higher than TC results. During a 5C discharge at an ambient temperature of 25 °C, a real-time temperature evolution obtained by the OFDR was presented in Fig. 15(c) in which the red dot along time domain was the instantaneous maximum temperature of the cell surface. It was obviously concluded that the location of the hotspot would vary during operation and the simplified movement of it was illustrated in Fig. 15(d).

3.2. Strain measurement

During charging and discharging processes of Li-ion batteries, strain evolution is monitored either by attaching the FBG sensors on the surface of the battery cell or by embedding the FBG sensors into the battery anode. Furthermore, novel structure is proposed to enhance the sensitivity of the FBG sensors. Li-ion pouch cell is the most popular type to be used in experiments while Li-ion coin cell is only employed to demonstrate the preliminary studies. Similarly, the research results are presented by publication time based on different research groups.

Sommer et al. [52] investigated the strain relaxation processes that occur after switching from charge to no-load phases by using optical fibre sensors in 2015. The strain was resulted from the change of electrode volume, due to the constant Li^+ fluctuation and intercalation from and to the positive electrode, and thermal expansion/contraction during charging and discharging processes. Thus, two FBG sensors were employed in the experimental setup, one, bonded at two points to the surface of the pouch cell with epoxy, responded to both strain and temperature variations; while the other one, loosely attached to the cell skin with a heat conducting paste, only related to temperature variations. The relationship between strain relaxation and SoC level was investigated. The results showed that strain relaxation was easier observed at higher SoC levels, especially strain signal relaxed by ~30 % at SoC level of 100 %, and the ratio of Li-ions in the outer electrode region to Li-ions in the inner electrode region was larger at a higher SoC level. The relationship between them was also investigated at various temperatures. It concluded that the residual strain increased with decreasing temperature for a certain SoC level and the difference between the residual strains was higher at a higher SoC level. Subsequently, Bae et al. [98] from the same research group developed two approaches to monitor the strain and stress evolution in the graphite anode of a small-format Li-ion pouch cell, as shown in Fig. 16(a) and Fig. 16(b). The attached approach embedded the FBG sensor between the graphite anode and the separator while the implanted approach integrated the FBG sensor entirely within the anode material. Measurements of the evolving strain and stress states of the graphite anode were conducted over charge-discharge cycles. The reflection spectra at 0 % and 100 % SoC of both the attached and the implanted FBG sensors were recorded in Fig. 16(c) and (d), respectively. Only monotonic peak shifting was detected in the attached FBG sensor, whereas both peak shifting and peak splitting were observed in the implanted FBG sensor. The reason, illustrated in Fig. 16(e) and (f), was that the attached FBG sensor was merely affected by the longitudinal strain due to the transverse strain was relieved by the compliant separator. However, because of the encapsulated configuration, the implanted FBG sensor was simultaneously affected by the longitudinal strain and the transverse strain which induced significant birefringence. Additionally, the implanted FBG sensor showed three times higher sensitivity than the attached FBG sensor at 100 % SoC. The total strain ε and stress σ were estimated by the equations in Ref. [98]:

$$\frac{\Delta\lambda}{\lambda_0} = \left\{1 - \frac{n_0^2}{2}[P_{12} - \nu(P_{11} + P_{12})]\right\}\varepsilon \tag{18}$$

$$\sigma = E\varepsilon \tag{19}$$

where λ_0 and $\Delta\lambda$ were the Bragg wavelength and the wavelength shift, respectively. n_0 was the average RI, $\nu = 0.19$ was the Poisson's ratio, $E = 69.9\ GPa$ was the Young's modulus, $P_{11} = 0.113$ and $P_{12} = 0.252$ were the respective strain-optical coefficients.

Fortier et al. [99] demonstrated a preliminary study on the integration of FBG sensor inside a Li-ion battery coin cell in 2017. In this study, the FBG sensor was integrated between the cathode and the separator layers as shown in Fig. 17(a) and Fig. 17(b). Optical-based NOA 65 was used as the sealant due to its longer life cycle and four layers of separator were implemented in the slotted coin cell to improve the functionality. The internal strain and the internal temperature were presented in Fig. 17(c) and (d), respectively. The results showed a strain stability within the cell over the charging cycle at a charging rate of C/20 and an approximately −79 με was recorded. The strain gradient was relatively small due to the small area of the coin cell. A temperature gradient between the internal cell temperature and the ambient temperature of approximate 10 °C was obtained over 50 h charge-discharge time.

Peng et al. [100] proposed a novel strain sensor based on FBG for Li-ion batteries in 2019. The structure of the strain sensor consisted of two FBGs (FBG I and FBG II), a sensitization structure and a protective cover, as shown in Fig. 18(a) while Fig. 18(b) gives the details of the sensitivity-enhanced structure, which contained two symmetrical lever mechanisms and an installation platform, in which the rotating pairs of levers were replaced by flexure hinges. In this strain sensor, FBG I (both ends were attached to the lever mechanism structure) was used as the functional grating and FBG II (left loose to avoid any stress drift) was acted as the thermal compensation grating. When the measured object was under strain ε then the strain on the FBG was ε_f, the total sensitivity enhancement coefficient was

$$K_T = \frac{\varepsilon_f}{\varepsilon} = \frac{l_2 l_4}{l_1 l_3} \cdot \frac{L}{L_f} \tag{20}$$

where L was the length between the two installation platforms, L_f was the length between the two fixed points on the grating, l_1, l_2, l_3, l_4 were the lengths of the lever arms as shown in Fig. 18(b) and (c). A comparison experiment between the proposed FBG sensor and a bare FBG sensor confirmed that the proposed sensor had an enhanced strain sensitivity which was 11.69 times larger than that of a bare FBG sensor with good linearity and repeatability.

Nedjalkov et al. [101] embedded a manufactured core FBG sensor into the anode plate of a 5 Ah Li-ion pouch cell to monitor strain condition in 2019. The manufactured core FBG had a length of 1 mm and 1200 RI variation points in the third grating period order with a reflectivity of 50 % at the central wavelength of 829 nm. In order to integrate the FBG inside the anode plate, a small groove was created by removing a central strip of the anode active material. The cell formation and cycling were conducted at 23.0 °C in a temperature-controlled chamber. The core FBG sensor exclusively detected the longitudinal expansion of the anode due to its structure. The results showed that during the cycling process, the maximum wavelength at the charging end decreased while the minimum wavelength at the discharging end increased, as shown in Fig. 19(a). The logarithmically plotted decay of the wavelength difference of a charging-discharging cycle was approximately linear to the linear capacity drop, as shown in Fig. 19(b). The SoC of the present battery cell can be indicated as

$$C[Ah] \approx \frac{ln\Delta\lambda[nm] + 18.7961[nm]}{5.7648[nm/Ah]} \tag{21}$$

where C was the residual discharge capacity and $\Delta\lambda$ was the wavelength

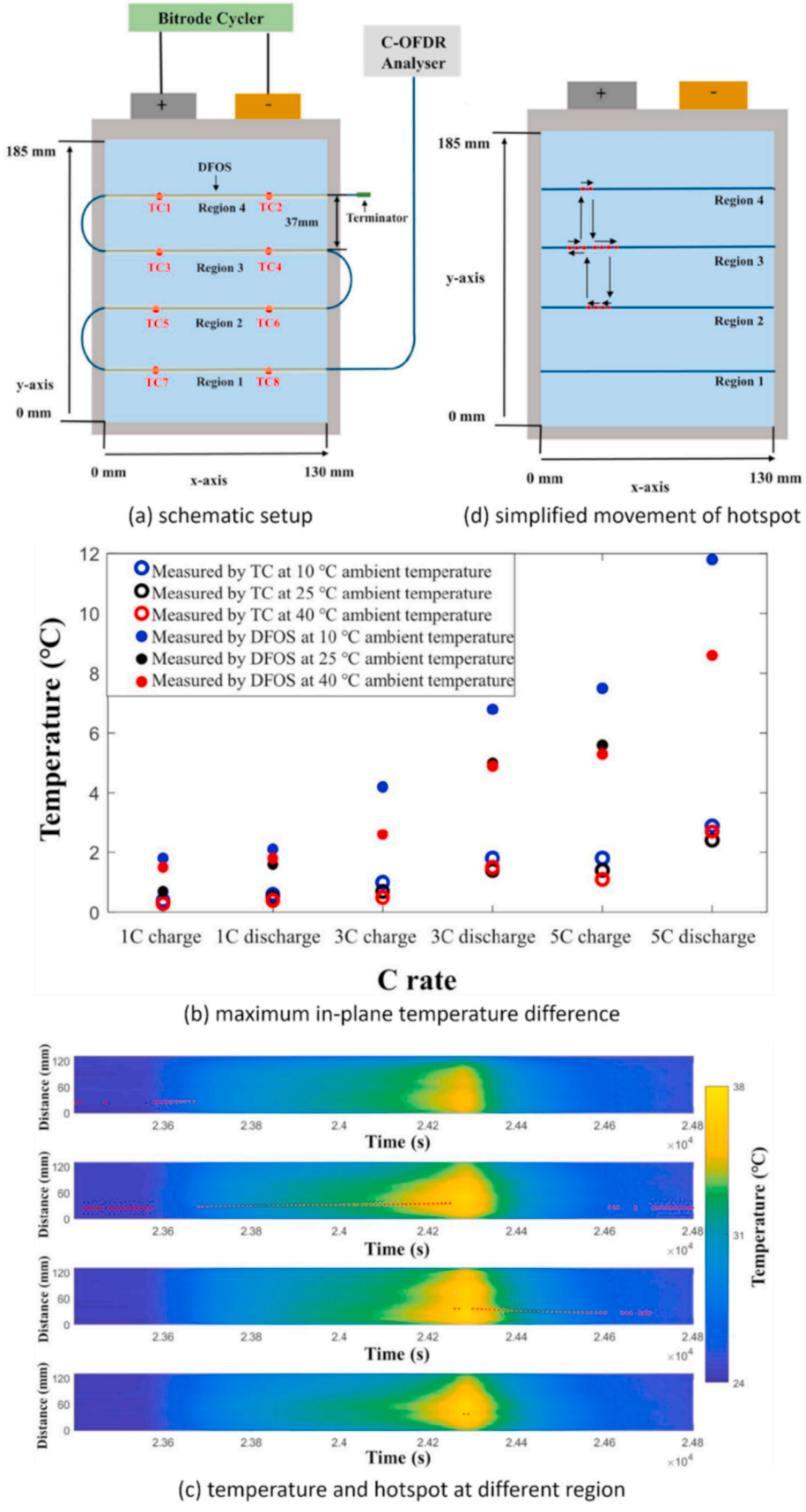

Fig. 15. Real-time distributed temperature monitoring of Li-ion battery. (a) schematic setup; (b) maximum in-plane temperature difference; (c) temperature and hotspot at different regions; (d) simplified movement of hotspot. Adapted from Ref. [42]. Copyright 2021.

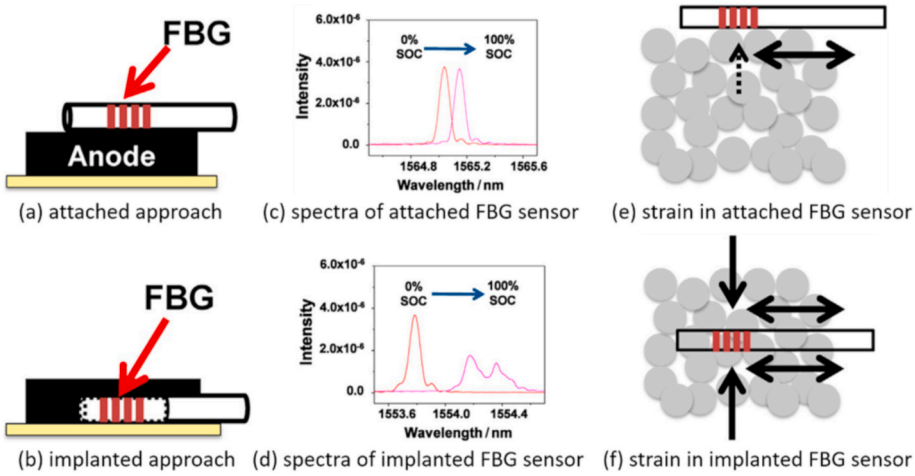

Fig. 16. Comparison of the two FBG sensors. Attached FBG sensor: (a) approach; (c) spectra at 0 % and 100 % SoC; (e) strain. Implanted FBG sensor: (b) approach; (d) spectra at 0 % and 100% SoC; (f) strain. Adapted from Ref. [98]. Copyright 2016.

difference of a full cycle.

3.3. Temperature and strain discrimination measurement

Strain evolution due in part to the temperature variations. Thus, some methods for discriminating temperature and strain have been proposed and demonstrated when the temperature and strain vary at the same time.

3.3.1. Reference FBG method

Nascimento et al. [32] employed FBG sensors to simultaneously monitor the temperature and bi-directional strain in a prismatic Li-ion battery in 2018, as shown in Fig. 20. The measurement was conducted by attaching two different types of FBG sensors to the Li-ion battery surface on both x- and y-directions. The strain-free FBG sensors (FBG1, FBG3 and FBG4), acted as references, were only used to measure temperature variations, while other FBG sensors (FBG2 and FBG5) were applied to simultaneously detect temperature and strain variations. The response wavelength shifts to temperature and strain were given as

$$\Delta\lambda_{B_1} = K_{T_1}\Delta T_1 \tag{22}$$

$$\Delta\lambda_{B_2} = K_{T_2}\Delta T_2 + K_{\varepsilon_2}\Delta\varepsilon_2 \tag{23}$$

where K_{T_1} was the temperature sensitivity of the strain-free FBG, K_{T_2} and K_{ε_2} were the temperature and strain sensitivities of the fixed FBG, respectively. ΔT and $\Delta\varepsilon$ were the temperature and strain changes, respectively.

The simultaneous temperature and strain variations registered by the FBG sensors placed on the two sides of the battery were recorded during discharge rates of 1.32C and 5.77C. The results showed that the maximum temperature and strain variations were obtained at the end of the CC charging process, with the values of 0.86 ± 0.13 °C on the negative electrode side, 29.61 ± 0.01 με and 122.49 ± 0.01 με on the x- and y-directions, respectively, during 1.32 C-rate. A deformation increase occurred due to the thermal expansion of the battery materials as the temperature increased. This research provided evidence of the effectiveness of the reference FBG method, enabling an alternative solution for real-time simultaneous sensing of temperature and strain.

3.3.2. Hybrid FBG-FPI method

Nascimento et al. [5] proposed a hybrid sensing network for the discrimination of internal strain and temperature in Li-ion batteries in 2019. The diagrams of the hybrid sensor and the experimental setup are illustrated in Fig. 21(a) and Fig. 21(b), respectively. The hybrid sensor consisted of an FBG sensor and an FPI sensor, the simultaneous measurements of temperature (ΔT) and strain ($\Delta\varepsilon$) were given as

$$\begin{bmatrix}\Delta\varepsilon\\ \Delta T\,\Delta T\end{bmatrix} = \frac{1}{K_{FP_\varepsilon}K_{FBG_T} - K_{FP_T}K_{FBG_\varepsilon}}\begin{bmatrix}-K_{FP_T} & K_{FBG_T}\\ K_{FP_\varepsilon} & -K_{FBG_\varepsilon}\end{bmatrix}\begin{bmatrix}\Delta\lambda_{FBG}\\ \Delta\lambda_{FP}\end{bmatrix} \tag{24}$$

where K_{FBG_T}, K_{FBG_ε} and $\Delta\lambda_{FBG}$ were the temperature sensitivity, strain sensitivity and wavelength shift of the FBG sensor, respectively. K_{FP_T}, K_{FP_ε} and $\Delta\lambda_{FP}$ corresponded to the FPI sensor.

The internal temperature and strain variations of three different positions (top, middle and bottom) during three different C-rates (0.5C, 1.0C and 0.25C) were obtained in the study. The results showed that the temperature increased more rapidly during the charging process in all cycles and the internal temperature variations (2.7 ± 0.1 °C) were higher than the external temperature variations (1.8 ± 0.1 °C) during the lower C-rate (0.3C). The strain variations were recorded as ~20.0 ± 0.1 με at the end of CC charge step and as 13.0 ± 0.1 με during the discharging process. Noted that all the strain variations were related to the temperature variations and the results showed that the higher strain variations were resulted from the higher temperature variations. Comparing the performance of the three different positions, it was found that the maximum absolute strain variations, 65.0 ± 0.1 με compared with 20.0 ± 0.1 με and 38.0 ± 0.1 με, were detected in the bottom while the maximum absolute temperature variations were obtained in the middle with the value of 3.3 ± 0.1 °C compared with 2.7 ± 0.1 °C and 2.5 ± 0.1 °C. The study proved the validity and feasibility of the proposed temperature and strain discrimination method.

3.4. RI measurement

Li-ion batteries primarily employ liquid electrolytes to ensure rapid ion transport for a high performance, the changes in the RI of the electrolytes are related to the changes in the conductive salt concentrations, thus the RI variations can be treated as indicator to the degradation progress. Nedjalkov et al. [101] proposed a novel-designed optical fibre sensor, named the self-compensating FBG sensor, to monitor the separator internal status of a Li-ion battery by detecting the RI of the battery electrolyte in 2019. The proposed FBG sensor consisted of a surface FBG and a cladding FBG that are schematically presented in Fig. 22(a). The surface FBG (orange), a sigmoid waveguide which was tangentially parallel to the fibre core at the beginning and parallel to the edge at the end, was inscribed into the fibre outer cladding which was gently etched to increase the sensitivity for RI variations. The cladding FBG (magenta), an additional waveguide positioned at half the distance between the fibre core and cladding surfaces in radial direction, was integrated into

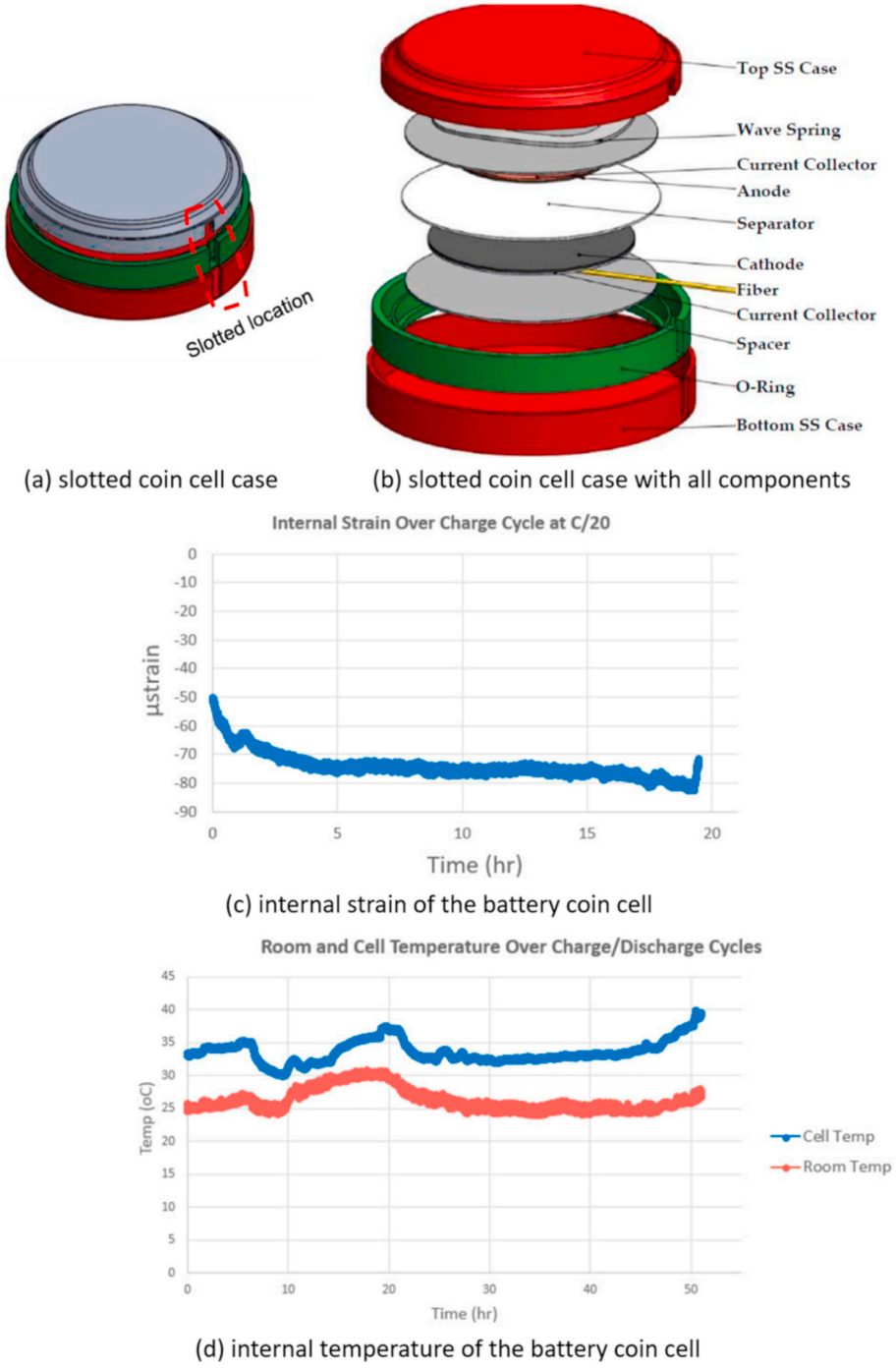

Fig. 17. FBG sensor integrated in a Li-ion battery coin cell. Schematic of the slotted coin cell (a) case and (b) all components; internal (c) strain and (d) temperature of the battery coin cell. Adapted from Ref. [99]. Copyright 2017.

the inner cladding at the same axial position. Both the influences of the longitudinal strain and temperature could be compensated with this configuration, thus the remaining variable of the measurement was the influence of the effective RI, which was proportional to the reflected Bragg wavelength shift. During the monitoring, the proposed FBG sensor was inserted centrally between two separator layers of a 5 Ah Li-ion pouch cell. The results of two exemplary cycles are shown in Fig. 22 (b) and (c), in which the green labels represent the signal dominantly influenced by the effective RI of the battery electrolyte.

3.5. Electrolyte density measurement

It is known that the electrolyte density decreases during the discharging process and increases during the charging process in lead-acid batteries, therefore, the evolution of the electrolyte density is a good indicator of SoH. In addition, stratification is created during the charging process due to the density difference between sulphuric acid and water, it thus requires the electrolyte density to be measured at different depths. Cao-Paz et al. [40] demonstrated a multi-point sensor based on U-shape fibre to measure the electrolyte density in lead-acid batteries in 2010. The multi-point sensor used in the study consisted of 5 optical fibres which were placed on the U-shape mould with a radius

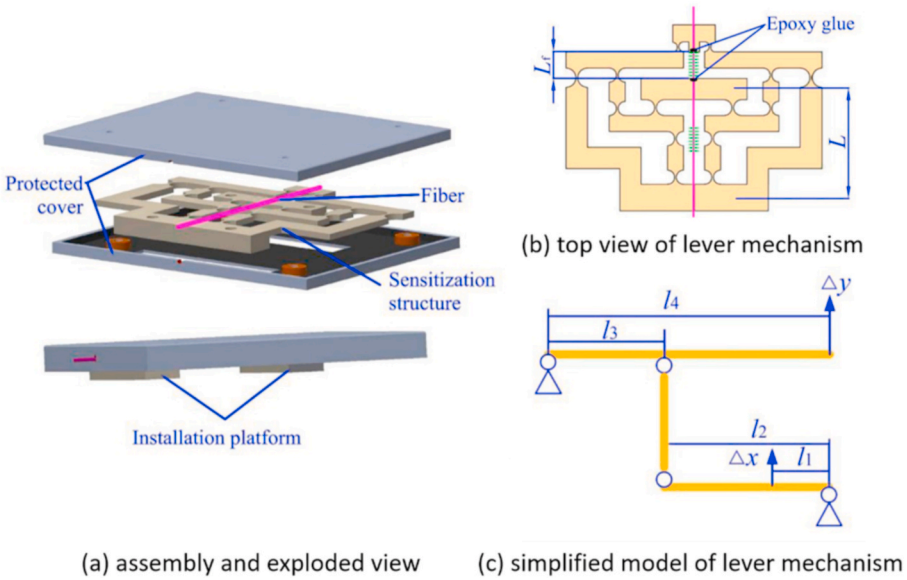

Fig. 18. Structure of the sensitivity-enhanced FBG sensor. (a) assembly and exploded view; (b) top view of lever mechanism; (c) simplified model of lever mechanism. Adapted from Ref. [100]. Copyright 2019.

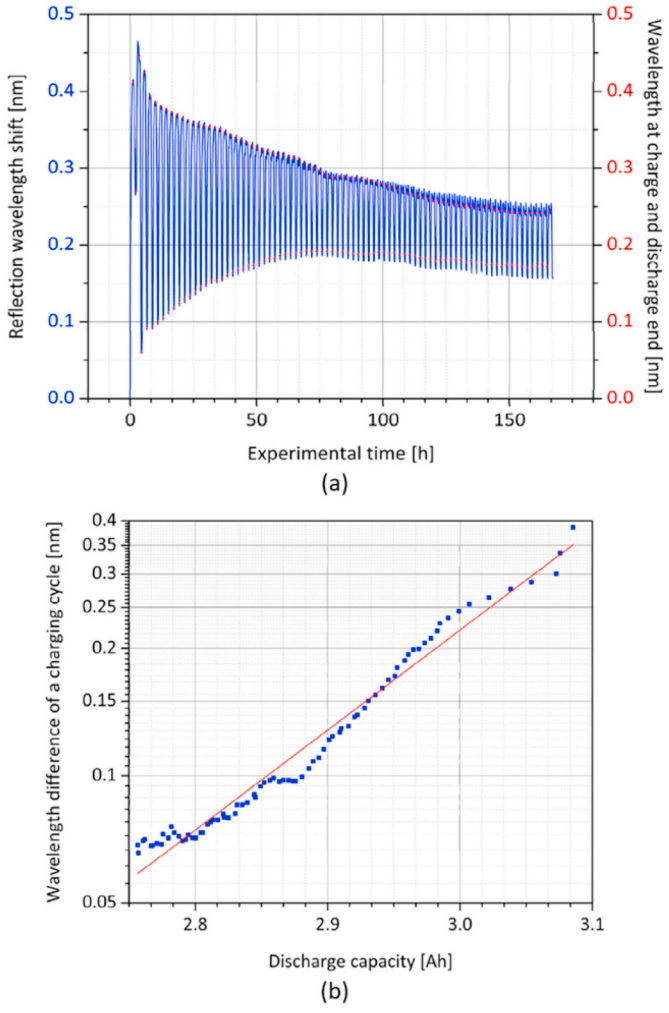

Fig. 19. Optical signal of the core FBG sensor. (a) reflection wavelength shift (left) and wavelength at charging and discharging end (right) during cycling process; (b) relationship between the wavelength difference and the discharge capacity. Adapted from Ref. [101]. Copyright 2019.

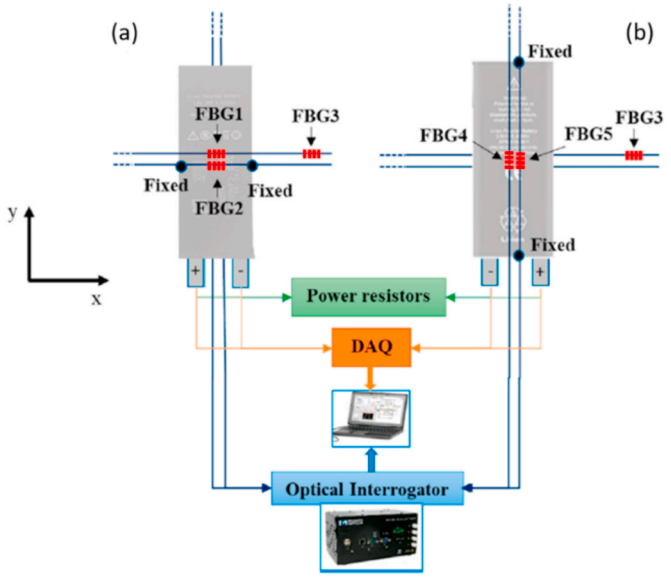

Fig. 20. Experimental diagram of the reference FBG method. (a) down view; (b) top view [32]. Copyright 2018.

length of 1.5 mm, as shown in Fig. 23(a). Among the 5 fibres, one of them was used as the reference fibre while the others worked as the sensing fibre. In order to monitor the electrolyte density at different heights at the same time, the lead-acid battery was divided into four zones (top zone, upper zone, medium zone and bottom zone) in each of which placed a sensing fibre (Fig. 23(b)). The evolution of the electrolyte density was observed during the charging process and five phases was distinguished in Fig. 23(c). The electrolyte density at different heights was obtained in real time, as presented in Fig. 23(d), making it possible to estimate the real-time SoC of the lead-acid battery. Furthermore, the top fibre was also used as a liquid level sensor to monitor the level of electrolyte in real time, it helped to carry out preventive maintenance of the battery.

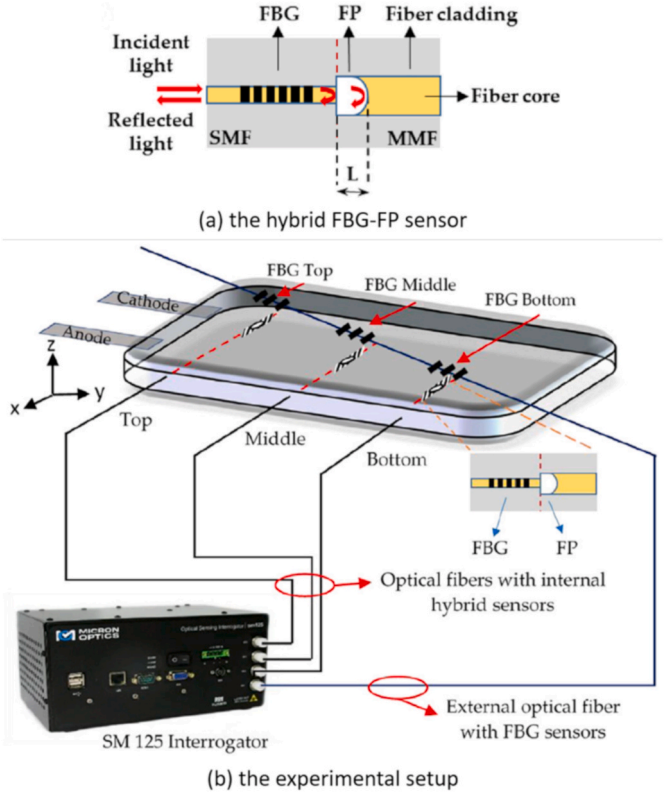

Fig. 21. Diagram of (a) the hybrid FBG-FP sensor and (b) the experimental setup. Adapted from Ref. [5]. Copyright 2019.

3.6. Flow change measurement

Information of the internal flow distribution is of critical importance for flow batteries, it not only helps to ensure the smooth operation of the battery cell but also it is used as the early detection of dendrite formation inside the cell. Vidakovic et al. [102] designed an FBG-based sensor system to detect the internal flow changes and the flow distribution inside a zinc-nickel flow battery in 2019. The sensor system was installed inside a previously machined groove on the surface of the flow cell with the use of pre-strain. Among the 6 FBG sensors, FBG1H, FBG2H and FBG3H were fixed to the top side in the horizontal orientation while FBG1V, FBG2V and FBG3V were fixed to the bottom side in the vertical orientation, as shown in Fig. 24. The temperature sensitivities of the horizontal FBG sensors and the vertical FBG sensors were 99 p.m./°C and 94 p.m./°C, respectively. After conducting the flow measurements multiple times, the research concluded that the horizontal FBG sensors were more sensitive to the flow changes than the vertical FBG sensors and the FBG2H performed the highest sensitivity to the flow changes. Additionally, the research also showed that the utility and the sensitivity of the sensor system would significantly reduce when the pre-tensioning of the sensors lost.

3.7. Oxygen concentration measurement

To achieve a high power density, the lithium–air battery requires sufficient oxygen to be supplied into the porous cathode where the oxygen concentration drastically decreases as the current density increases during operation. It is crucial to understand and thus improve the oxygen transport phenomena in the porous cathode to obtain a more powerful aqueous lithium–air battery. Fujimoto et al. [88], for the first time, measured the oxygen concentration in the porous cathode of a lithium–air battery in 2019. As shown in Fig. 25(a), a fine optical fibre sensor was employed with platinum tetrakis pentafluorophenyl

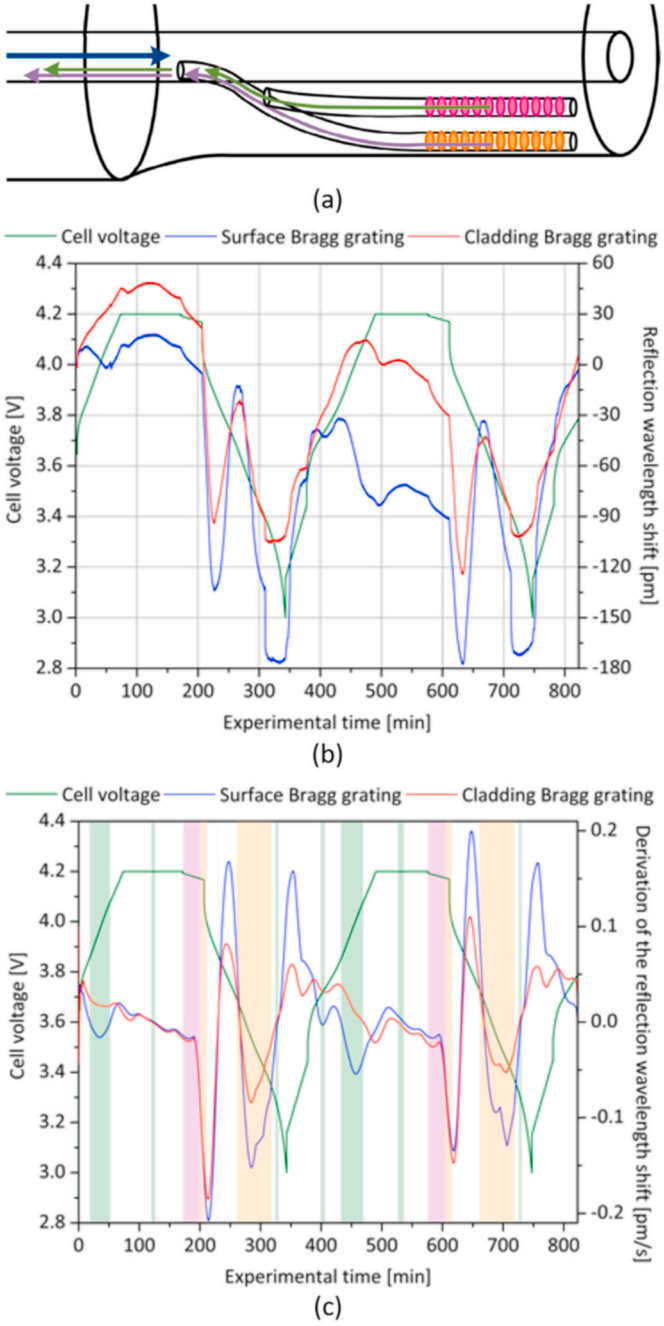

Fig. 22. RI measurement research. (a) schematic of the self-compensating FBG sensor; (b) electrical and optical signal of the Li-ion battery; (c) corresponding first derivation of the optical signal. Adapted from Ref. [101]. Copyright 2019.

porphine (PtTFPP), the oxygen indicator, painted on the edge of the optical fibre. It was known that a phosphorescence emission (650 nm) would occur when PtTFPP was exposed to the excitation light (405 nm) and the intensity of the phosphorescence changed at different oxygen concentration. Therefore, the oxygen concentration was obtained by measuring the phosphorescence intensity and using the Stern–Volmer equation

$$\frac{I_0}{I} = 1 + A \cdot [O_2] \tag{25}$$

where I_0 and I were the measured phosphorescence intensities without and with oxygen, respectively. A was a constant determined by the experiment and $[O_2]$ was the oxygen concentration.

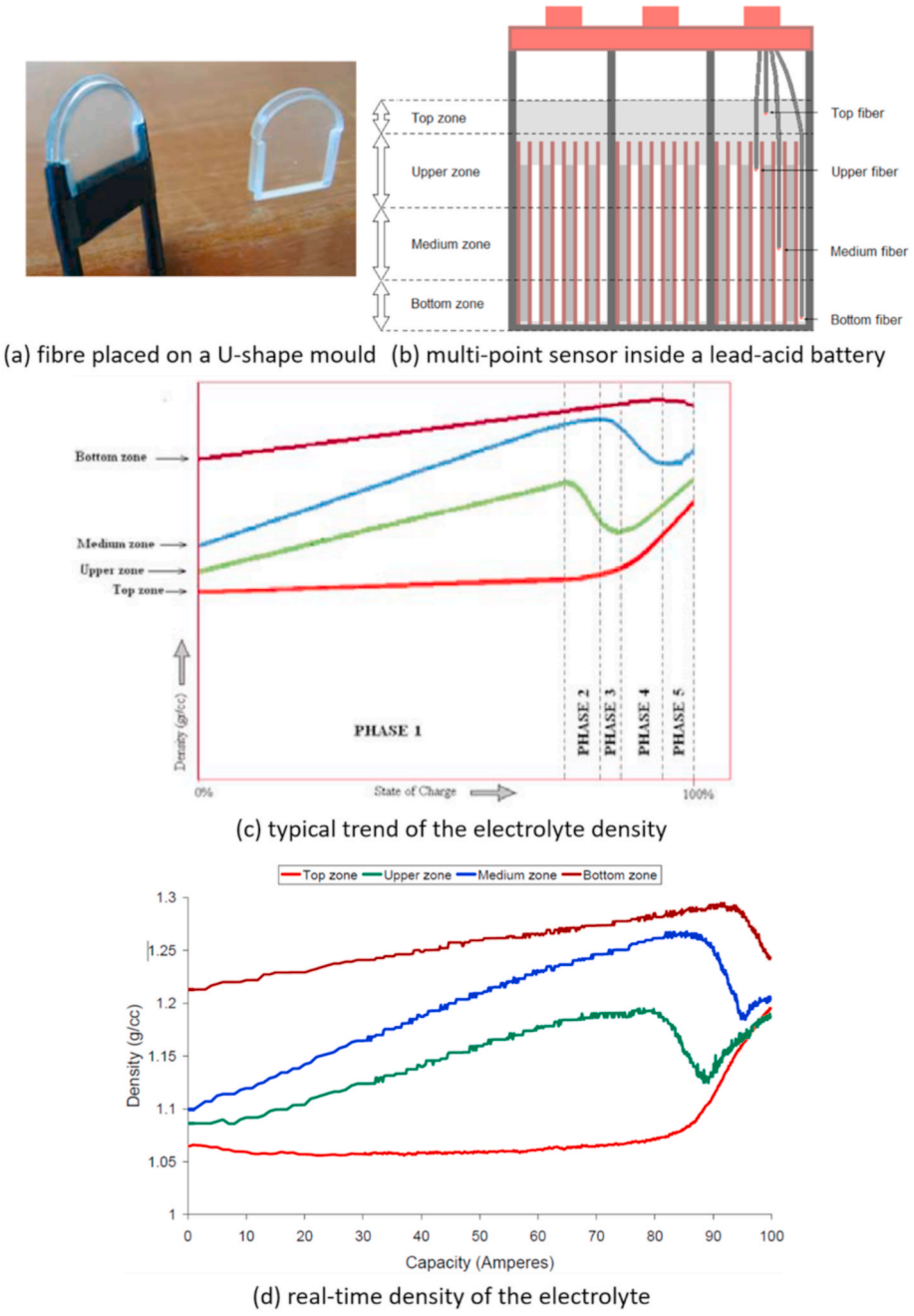

Fig. 23. A multi-point sensor based on optical fibre. (a) schematic of the U-shape fibre; (b) multi-point sensor inside a lead-acid battery with different zones; (c) typical trend of the electrolyte density; (d) real-time density of the electrolyte. Adapted from Ref. [40]. Copyright 2010.

The spatial and temporal oxygen concentration distribution at each current density was obtained and shown in Fig. 25(b). During the discharging process, the oxygen concentration in the porous cathode decreased with time and the rate of change increased with the increasing current density. Meanwhile, the lower electrolyte and the upper electrolyte presented the gradients of oxygen concentration. It also concluded that a thin upper electrolyte layer was necessary to obtain a sufficient oxygen transport from the air layer to the porous cathode.

3.8. SoC and SoH measurement

SoC and SoH, as two crucial factors reflecting the state of batteries, are commonly estimated under the assistance of the evanescent wave sensors in Li-ion batteries or supercapacitors. Moreover, the fibre grating sensors are combined with them to improve the sensing performance. In addition, the interferometer sensors are proposed to monitor SoC of VRFB recently. The results included herein of multiple research groups are continuously presented by publication time.

Ghannoum et al. [103] reported a study on the reflectance of the commercial graphite anodes in Swagelok Li-ion batteries and the optical fibre evanescent wave spectroscopy of electrochemically lithiated graphite in 2016. The results demonstrated a significant increase in the reflectance of the lithiated graphite in the near-infrared band (750–900 nm) as a function of SoC. A similar SoC dependent trend was observed in the transmittance when a fibre was embedded in the Swagelok cell. The study suggested that an embedded optical fibre sensor could be used to measure the SoC of a Li-ion battery. However, the significant lifespan decay and cell deformation of the prototype Swagelok cell limited the system performance. In order to develop a viable long-term monitoring system, a custom pouch cell was formed by them [104] in the same year.

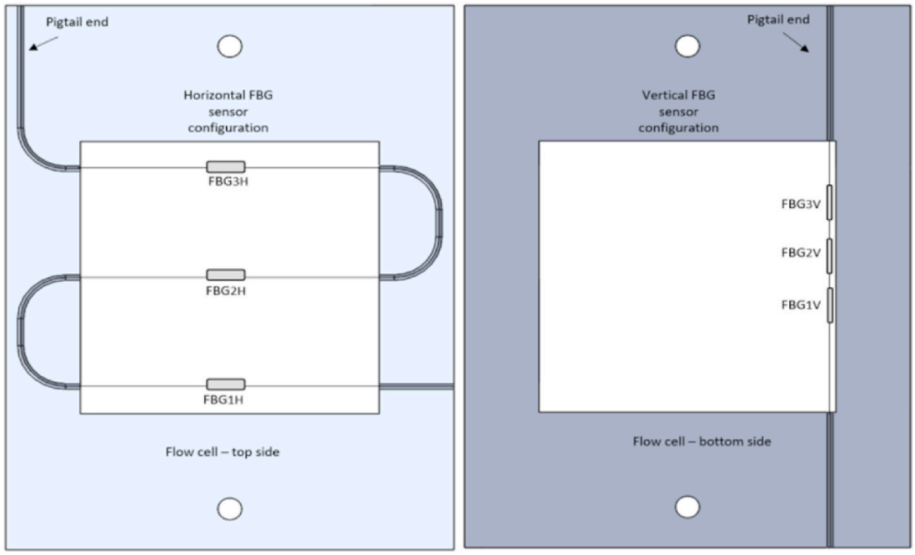

Fig. 24. FBG-based sensor system layout [102]. Copyright 2019.

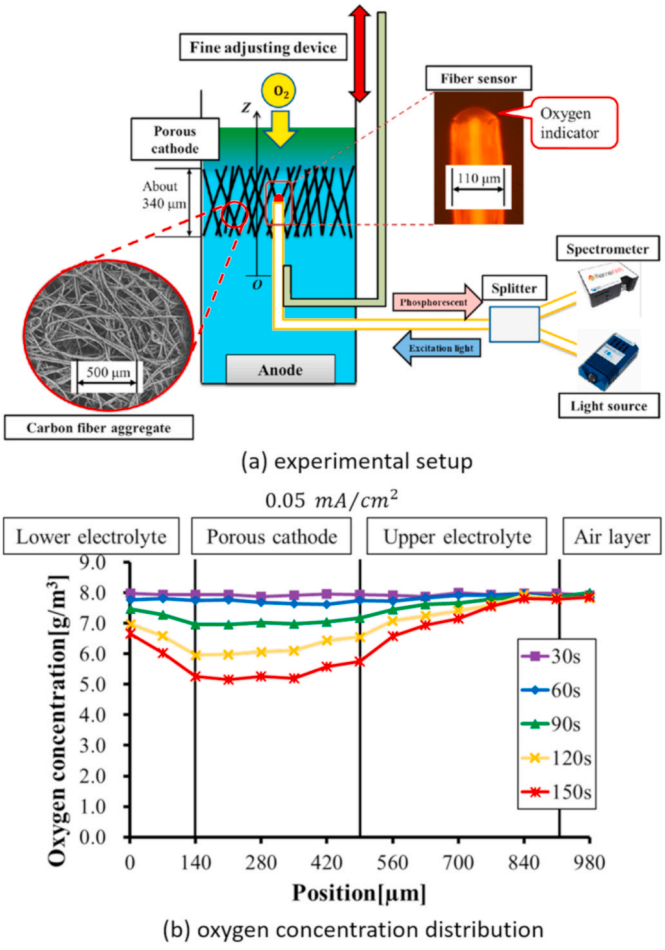

Fig. 25. Oxygen concentration measurement. (a) experimental setup; (b) oxygen concentration distribution. Adapted from Ref. [88]. Copyright 2019.

In this sensing system, the etched fibre was embedded between the graphite anode and the polymer separator of the pouch cell, the transmittance signal of the optical fibre sensor was observed in real time by an in-house optical sensor interrogator. After testing over multiple partial and full cycles, the results proved the ability to monitor the state of lithiation of the graphite and estimate the SoC of a Li-ion battery. Compared with [103], a significant performance improvement in the cycle efficiency was obtained from 72 % in the Swagelok cell to 89 % in the pouch cell. Later, the same research group [105] presented the fabrication and integration of the optical fibre sensor into a cylindrical Li-ion cell as well as a Li-ion pouch cell in 2017. A buffered HF solution of 7.0 *wt%HF* and 34.3 *wt%* NH_4F was proved to be superior in etching the optical fibre. It was also proved that the sensitivity of the sensor increased along with increasing the area that the sensor contacted within the graphite anode. The optical fibre evanescent wave sensor integrated into the graphite anode demonstrated the potential use to monitor the SoC and SoH of Li-ion batteries. The configurations of Li-ion cells embedded with the proposed sensor are presented in Fig. 26. Recently, Ghannoum et al. [106] conducted an analysis of the interaction between the optical fibre evanescent wave sensor and the graphite particles within a Li-ion battery in 2020. The results showed that the proposed optical fibre evanescent wave sensor was sensitive to lithium concentration at the surface of graphite particles, therefore, it was able to monitor the capacity fade of Li-ion batteries.

Lao et al. [33] proposed a novel method, named TFBG-based SPR optical fibre sensor, for the in-situ monitoring of the SoC of supercapacitors in 2018 for the first time. The configuration of the TFBG-based SPR optical fibre sensor is illustrated in Fig. 27(a), where a 50-nm-thick gold layer of high surface quality was deposited on the TFBG of which the tilt was 18° and an additional gold coating was deposited on the end of the fibre to achieve a single-ended sensor with interrogation in reflection. The proposed plasmonic TFBG sensor was attached to one of the electrodes of the supercapacitor to monitor the electrochemical activity, as presented in Fig. 27(c) which is the experimental setup. The charge density measurement and the SoC measurement were demonstrated in this research, the results showed that the

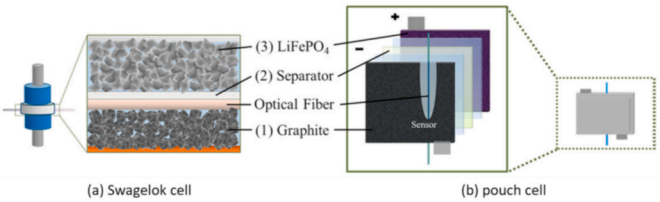

Fig. 26. The configurations of Li-ion cells. (a) Swagelok cell; (b) pouch cell. Adapted from Ref. [105]. Copyright 2017.

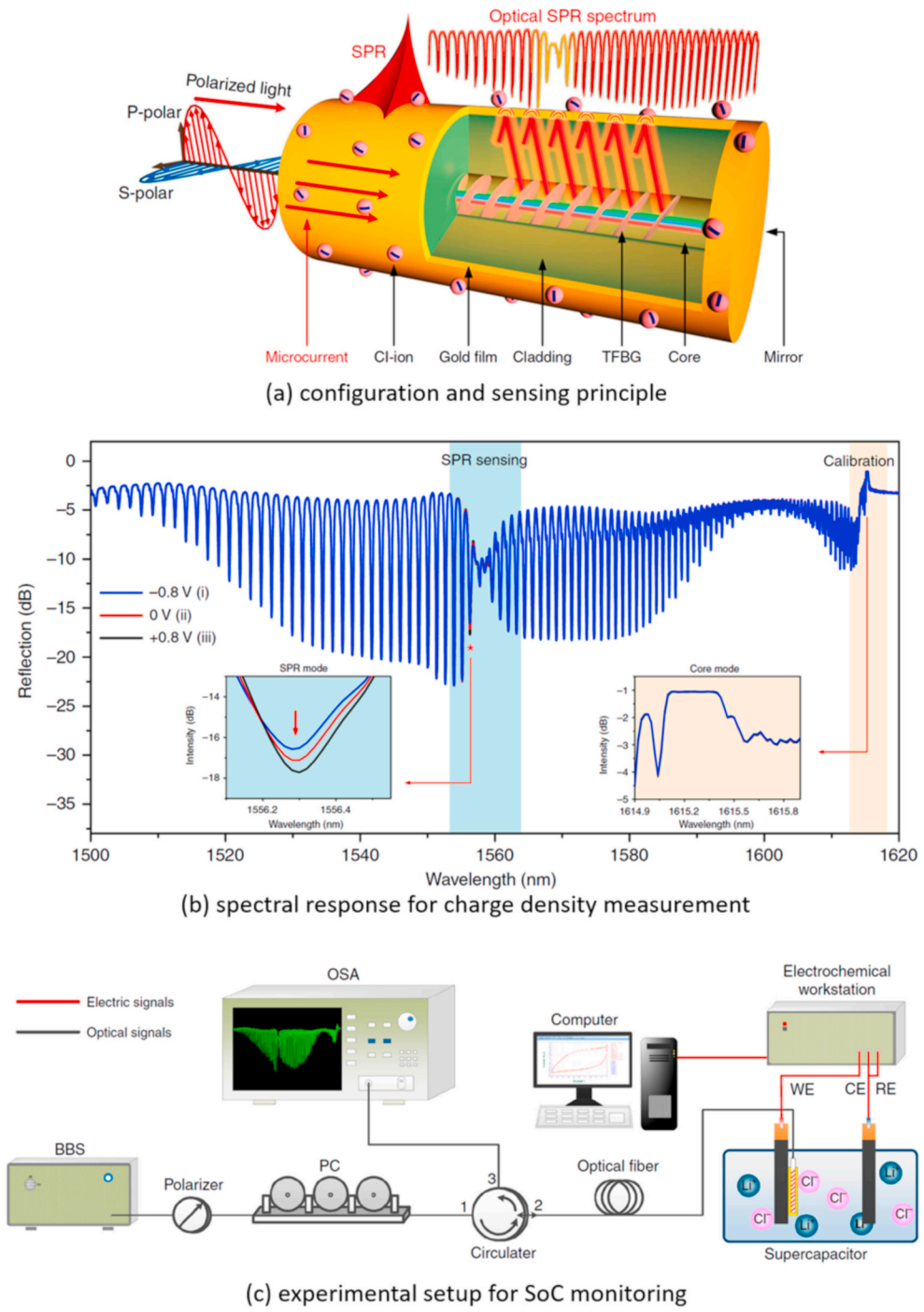

Fig. 27. TFBG-based SPR optical fibre sensor. (a) configuration and sensing principle; (b) spectral response for charge density measurement; (c) experimental setup for SoC monitoring. Adapted from Ref. [33]. Copyright 2018.

spectral response of the SPR mode of the TFBG was directly related to the charge density and the SoC of the supercapacitor, as shown in Fig. 27 (b). Therefore, the changes of the charge density and the SoC during the charging and discharging processes could be monitored by detecting the changes of the position and the intensity of the reflection spectrum.

Modrzynski et al. [107] presented an SoC measurement method based on an optical fibre sensing system in 2019. Two etched optical fibres were embedded in both graphite anode and lithium iron phosphate with the addition of indium tin oxide cathode of a Li-ion pouch cell. The SoC was measured in real time by simultaneously monitoring the light transmission through both the fibres. The results showed that the SoC correlated transmission behaved similarly for both electrodes. However, different relaxation behaviours and wavelength dependent behaviours were observed during the charging and discharging processes. The study proved that the optical fibre sensing method was able to estimate the SoC independent of the electrical measurement methods.

Qian et al. [108], for the first time, proposed a method based on localized surface plasmon resonance (LSPR) for the SoC monitoring of supercapacitor in 2020. As shown in Fig. 28(a), the Au nanoparticles were deposited on the fibre core of a multimode optical fibre to create the LSPR sensing area (10 mm) and a silver reflective mirror was coated at the end of the optical fibre (2 mm). In order to monitor the SoC, a three-electrode supercapacitor was used as shown in Fig. 28(b), where Ag/Ag/Cl performed as the reference electrode (RE), Pt as the counter

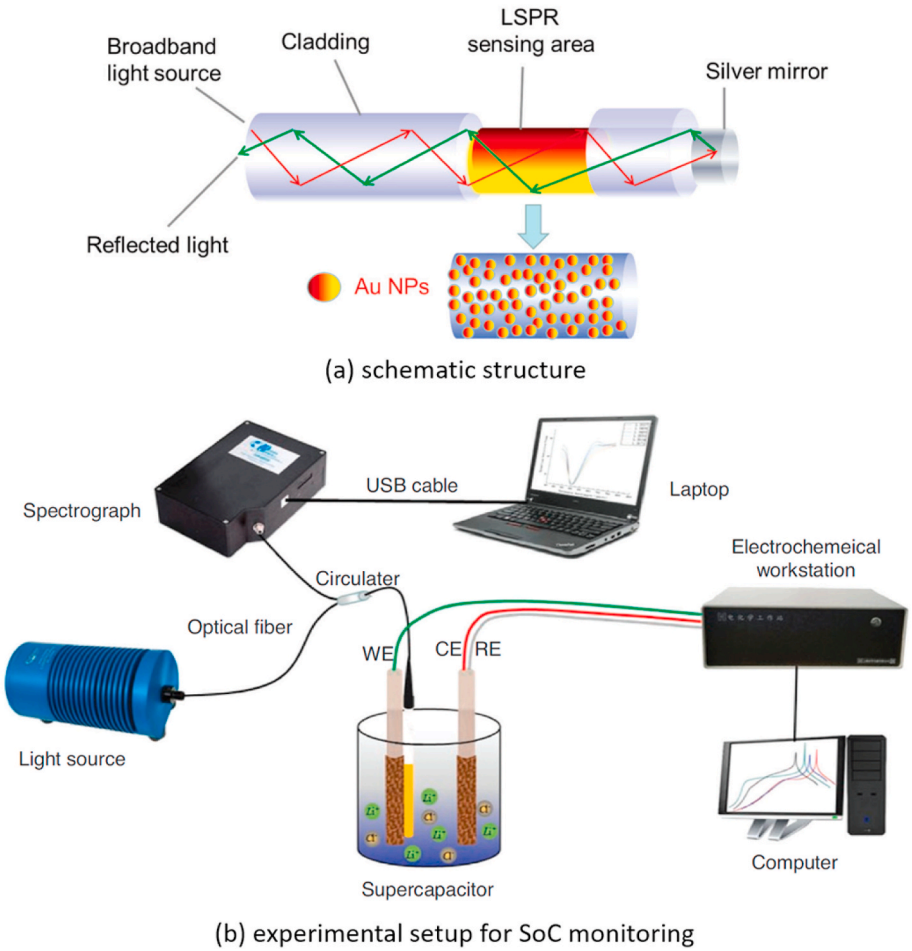

Fig. 28. LSPR optical fibre sensor. (a) schematic structure; (b) experimental setup for SoC monitoring. Adapted from Ref. [108]. Copyright 2020.

electrode (CE) and carbon fabric-based MnO_2 as the working electrode (WE) near which the LSPR optical fibre sensor was hooked. The LSPR sensor was demonstrated for real-time online SoC monitoring of the electrode in the supercapacitor during the charging and discharging processes. The intensity shift of the LSPR spectrum was found to have a good linear relationship with the SoC of the electrode and an SoC sensitivity of $3.2 \times 10^{-3}\%/mC$ was obtained. However, no temperature sensitivity was observed.

Ma et al. [109] proposed a novel scheme for the SoC monitoring for the VRFB in 2020. The sensor was based on an air-gap fibre Fabry–Perot interferometer (AGFFPI) which consisted of two single-mode fibre and an air gap of 43 μm, as shown in Fig. 29(a). It was known that the SoC of a VRFB with identical quantities of electrochemically available V ions was

$$SoC = \frac{V^{5+}}{V^{5+} + V^{4+}} \times 100\% = \frac{V^{2+}}{V^{2+} + V^{3+}} \times 100\% \quad (26)$$

During an ideal charging process, the increase of the SoC led to a linear increase in the percentage of V^{5+} or V^{2+}, as well as a linear decrease in the H_2O concentration and H^+ concentration of the positive electrolyte, which further resulted in a linear decrease of the RI of the positive electrolyte. Additionally, the relationship between the variation in RI (Δn) and the interference spectrum shift ($\Delta\lambda$) was also linear, therefore, the SoC was linearly proportional to $\Delta\lambda$ of the AGFFPI. Fig. 29 (b) shows the experimental setup implemented for SoC monitoring. The research concluded a mathematical relationship between SoC and $\Delta\lambda$ as

$$SoC(\%) = \frac{\Delta\lambda - m_{T,ave} \cdot (T - 25)}{m_{SoC}} \quad (27)$$

where T was the temperature of electrolyte, $m_{T,ave}$ was the average sensitivity of $\Delta\lambda$ with respect to T under different SoC levels, m_{SoC} was the sensitivity of $\Delta\lambda$ with respect to SoC at 25 °C. According to the measurement results, an SoC estimation error of 0.57 % was obtained.

As seen in Table 2, the battery sensing performance reviewed above is summarized in terms of the publication time, the corresponding battery technology, sensing parameter and deployed optical fibre sensing technology are listed as well.

4. Challenges and outlooks

With the rapidly expanding battery energy storage technology, the development of various battery sensing systems has shown to be crucial in both academia and industry. Currently, the field of optical fibre sensing for batteries is moving beyond lab-based measurement and is increasingly becoming implemented in the in situ monitoring to help improve battery chemistry and assist the optimisation of battery management [4,6]. However, several challenges still remain to advance the development of optical fibre sensing systems for batteries in the future.

Firstly, implementing the optical fibre sensors in real batteries, including cells, modules and packs, is the first challenge without influencing both batteries' and optical fibres' performance. As discussed beforehand, for accurately monitoring and estimating battery performance, the internal information which requests the sensors to be embedded in batteries is more precise than the external information. The use of optical fibres has shown to have a high stability and tolerance to the inner electrochemical environment of batteries without the risks of electrically conducting, electro-magnetic interference, radio

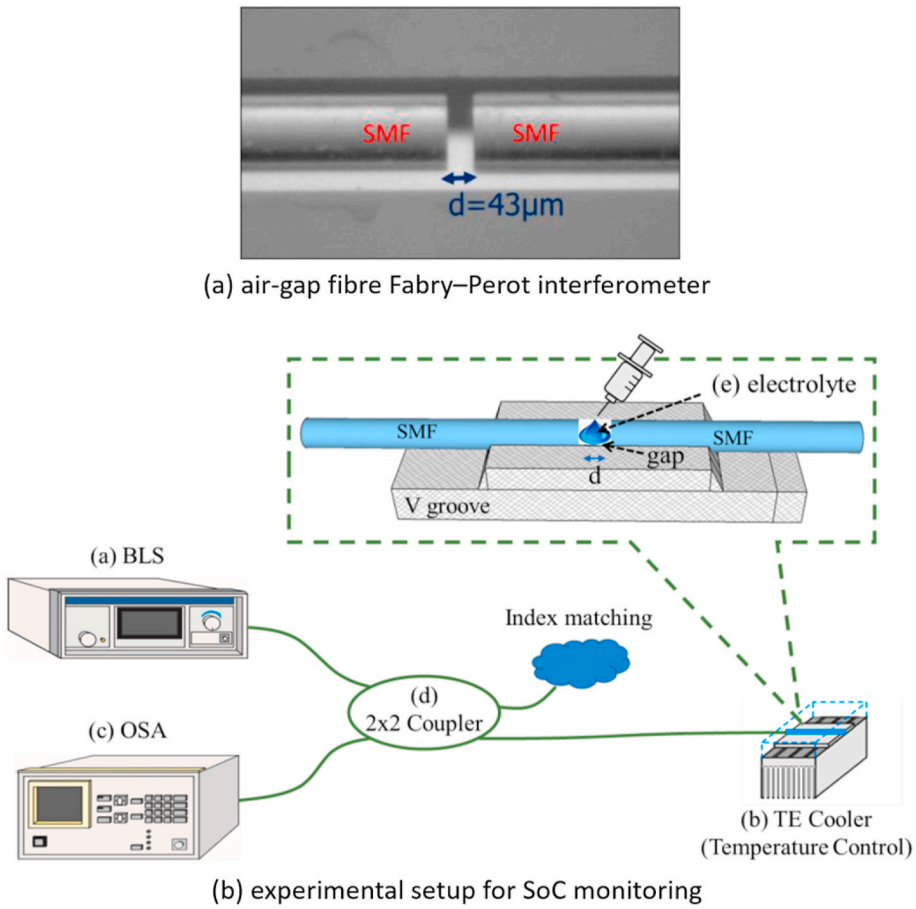

Fig. 29. AGFFPI optical fibre sensor. (a) structure of the AGFFPI; (b) experimental setup for SoC monitoring. Adapted from Ref. [109]. Copyright 2020.

Table 2
Summarization of battery sensing performance.

Year	Researcher	Battery technology	Sensing parameter	Sensing technology	Resolution/Accuracy	Ref.
2010	Cao-Paz et al.	Lead-acid	Electrolyte density	Optical Fibre Evanescent Wave	–	[40]
2011	Du et al.	Li-ion	Temperature	Fluorescence Lifetime Measurement	0.5 °C	[41]
2013	Yang et al.	Li-ion	Temperature	FBG	0.1 °C	[48]
2015	Sommer et al.	Li-ion	Strain	FBG	–	[52]
2016	Iyer	Li-ion	Temperature & SoC	Evanescent Field Fluorescence + Fluorescence Intensity Measurement	0.168/0.86 °C	[86]
2016	Novais et al.	Li-ion	Temperature	FBG	0.1 °c	[39]
2016	Bae et al.	Li-ion	Strain	FBG	–	[98]
2017	Fortier et al.	Li-ion	Temperature & Strain	FBG	–	[99]
2018	Nascimento et al.	Li-ion	Temperature & Strain	FBG	0.13 °C/0.01 με	[32]
2018	Fleming et al.	Li-ion	Temperature	FBG	1 °C	[96]
2019	Nascimento et al.	Li-ion	Temperature	FBG	0.1 °c	[35]
2019	Nascimento et al.	Li-ion	Temperature & Strain	FBG + FPI	0.1 °C/0.1 με	[5]
2018	Lao et al.	Supercapacitor	SoC	TFBG + SPR	–	[33]
2019	Vergori et al.	Li-ion	Temperature & Strain	OFDR	1.3 mm	[97]
2019	Peng et al.	Li-ion	Strain	FBG	–	[100]
2019	Nedjalkov et al.	Li-ion	Strain & RI	FBG	–	[101]
2019	Vidakovic et al.	Zinc-nickel	Flow change	FBG	–	[102]
2019	Fujimoto et al.	Lithium-air	Oxygen concentration	Phosphorescence Intensity Measurement	–	[88]
2019	Modrzynski et al.	Li-ion	SoC	Light Transmission	–	[107]
2020	Ghannoum et al.	Li-ion	SoC/SoH	Optical Fibre Evanescent Wave	–	[106]
2020	Qian et al.	Supercapacitor	SoC	LSPR	$3.2x10^{-3}$%/mC	[108]
2020	Ma et al.	VRFB	SoC	FPI	–	[109]
2021	Yu et al.	Li-ion	Temperature	OFDR	1.3 mm	[42]

frequency interference and corrosive chemical species. However, it is vulnerable to sharp bending and vibration [110]. Thus, the deployment strategy where the fibre is embedded in a battery cell should be taken into consideration. Although a reflection-based configuration is preferred for battery cells due to the simplified sealing process and minimised risk of electrolyte leakage [111], the one-entry configuration is not suitable for the battery modules and packs. Thus, the implementation of optical fibre sensors being attached on or embedded in battery modules and packs still needs to be carefully designed depending on the mechanical and optical characteristics. As the research

progresses, volume manufacturing and automation of instrumented batteries with optical fibres will be an important area to investigate. Besides, the cost of optical fibre sensors limits their implementation in practical battery systems, especially cell-level system. Therefore, this requires further development of the optical sensing methods in a cost-effective way compatible with industrial manufacturing processes as well.

Secondly, the scale-up and deployment of optical fibre sensors from cell level to module and pack applications need to be addressed. Substantial deployments of optical fibre sensors for various cell formats based on different chemistries have been discussed in previous sections. The intrinsic chemical, mechanical and thermal robustness suggests that the operando techniques explored in this review can be extended to other energy storage devices, such as fuel cells and supercapacitors, to achieve fundamental advancements in cell characterisation and system management. Moreover, the optical fibre sensors have risen to one of the most viable alternative to traditional electrical sensors in a wide range of battery applications, especially in automotive and grid-scale battery systems, where large format battery cells are usually deployed to form modules and packs. In automotive applications, the battery modules assembled by a single series string or a series-parallel arrangement of battery cells are combined electrically to form a battery pack whose size and shape are decided by the dimensions of the vehicle to provide the full power and energy need for the EVs [112,113]. In grid-scale energy storages applications, modular racks [114] or battery pods [115] are integrated to build a grid-scale site. In these battery systems, take temperature monitoring as an example, not only the gradient between the internal and external temperatures in a large format battery cell, but also the temperature differences between adjacent cells are crucial to avoid accelerated degradation or possible safety concerns. Consequently, appropriate deployment strategies of optical fibre sensors for monitoring modules and packs are of great interest in the future.

Thirdly, the control strategies to support in-situ use within a BMS in addition to characterisation also need to be addressed. An advanced BMS with excellent performance requires the sensing system to provide reliable and accurate input measurement data for the algorithms which perform battery modelling, parameter identification, estimation and prediction of battery states, such as SoC and SoH [116]. Currently, the BMS algorithms, both traditional and intelligent, have inputs such as primary current and cell voltage, the temperature of the cells, ambient temperature as well as the temperature at the battery coolant inlet and outlet [117,118]. However, the optical-related information, such as high resolution spatially distributed measurements of temperature and mechanical load are not available. The lack of connection between the optical fibre sensing systems and the BMS algorithms results in inaccuracy and a time-consuming convergence rate. Therefore, interfaces and communication between optical fibre sensors and BMS must be addressed to enable the measured information to be transmitted to the BMS. Within the context of BMS integration, research is underway to design bespoke electronics hardware to perform in-situ fibre optics operations. The electronics may be integrated with the BMS hardware or be installed within the final application and communicate with the BMS via an appropriate network technology, such as an ethernet, Controller Area Network (CAN) or Serial Peripheral Interface (SPI).

Lastly, multi-functional optical fibre sensing using a single optical fibre to assist BMS forms another challenge. One indispensable requirement of the battery sensing system is to provide multi-dimensional information for the next-generation BMS [116,119]. Not only the traditional battery electrical- and thermal-related information (voltage, current and temperature), but also the battery electrochemical- (impedance/resistance, ion concentration, gas), mechanical- (strain/-stress), acoustical- (intensity) and optical- (intensity, frequency and phase) related information will be significant to the innovation of intelligent battery sensing and the development of new state estimation algorithms. Although the existing optical fibre sensing technologies discussed in this review can realise the monitoring of various parameters, simultaneous multiple sensing system is one of the trends in intelligent battery sensing. A feasible solution is to integrate different optical fibre sensors into the same fibre to achieve multiplexed measurements. In addition, distributed optical fibre sensing methods could be developed into advanced optical fibre sensors capable of measuring temporally and spatially multiple parameters simultaneously with high sensitivity and accuracy.

Overall, the mathematical modelling, engineering and manufacturing communities will benefit from the measurement data derived from the use of optical fibre sensors. Fibre optics can be applied in various stages of studies, ranging from supporting the design of new cells, design of thermal management systems, mathematical model development and parametrisation of the model, supporting safety evaluation and battery performance assessment. The convergence of battery science and optical fibre sensor engineering will significantly improve battery safety, reliability, performance and lifetime.

5. Conclusions

This paper presents a review of all the main optical fibre sensing methods being developed for batteries. According to the operating principles, the optical fibre sensors cover the five types, namely optical fibre grating sensors, optical fibre interferometer sensors, optical fibre evanescent wave sensors, optical fibre photoluminescent sensors and optical fibre scattering sensors. All which have been investigated by researchers on the measurement of different battery parameters, such as temperature, strain, RI, electrolyte density, flow change, oxygen concentration, SoC and SoH.

Among the five types, optical fibre grating sensors, optical fibre interferometer sensors and optical fibre photoluminescent sensors are popularly employed in physical parameter sensing while optical fibre evanescent wave sensors are generally used for electrochemical parameter monitoring. Nevertheless, the sensing methods presented in this paper are often implemented in a fusion way. Furthermore, other than the optical fibre scattering sensor of which uses a distributed sensing method, all other four types above are pointwise sensors. This results in the scattering sensor to be the most promising optical fibre sensing method for batteries in the future.

Declaration of competing interest

The authors declare that they have no known competing financial interests or personal relationships that could have appeared to influence the work reported in this paper.

Acknowledgements

This work was funded by High Value Manufacturing Catapult, grant reference, 160080 CORE (WMG), titled ‘Smart Sensing for Future Batteries’ and the EPSRC (Engineering and Physical Sciences Research Council), grant reference EP/R004927/1, titled ‘Prosperity Partnership’. The author Gaoce Han would like to acknowledge the China Scholarship Council for sponsoring. The permission is attained for all copyrighted figures.

References

[1] Alotto P, Guarnieri M, Moro F. Redox flow batteries for the storage of renewable energy: a review. Renew Sustain Energy Rev 2014;29:325–35. https://doi.org/10.1016/j.rser.2013.08.001.
[2] Pistoia G. Lithium-ion batteries: advances and applications. Newnes; 2014. https://doi.org/10.1016/C2011-0-09658-8.
[3] IRENA. Electricity storage and renewables: costs and markets to 2030. Electricity-Storage-and-Renewables-Costs-and-Markets 2017:132.
[4] IEA. Innovation in batteries and electricity storage. 2020.
[5] Nascimento M, Novais S, Ding MS, Ferreira MS, Koch S, Passerini S, et al. Internal strain and temperature discrimination with optical fiber hybrid sensors in Li-ion

batteries. J Power Sources 2019;410–411:1–9. https://doi.org/10.1016/j.jpowsour.2018.10.096.
[6] Edström K. Battery 2030+ roadmap. 2020.
[7] Raijmakers LHJ, Danilov DL, Eichel RA, Notten PHL. A review on various temperature-indication methods for Li-ion batteries. Appl Energy 2019;240:918–45. https://doi.org/10.1016/j.apenergy.2019.02.078.
[8] Mutyala MSK, Zhao J, Li J, Pan H, Yuan C, Li X. In-situ temperature measurement in lithium ion battery by transferable flexible thin film thermocouples. J Power Sources 2014;260:43–9. https://doi.org/10.1016/j.jpowsour.2014.03.004.
[9] Goutam S, Timmermans J, Omar N, Bossche P Van Den, Mierlo J Van, Rodriguez L, et al. Surface temperature evolution and the location of maximum and average surface temperature of a lithium-ion pouch cell under variable load profiles. Euroepan Electr Veh Congr 2014:1–7.
[10] Bolsinger C, Birke KP. Effect of different cooling configurations on thermal gradients inside cylindrical battery cells. J Energy Storage 2019;21:222–30. https://doi.org/10.1016/j.est.2018.11.030.
[11] Zhao R, Zhang S, Gu J, Liu J, Carkner S, Lanoue E. An experimental study of lithium ion battery thermal management using flexible hydrogel films. J Power Sources 2014;255:29–36. https://doi.org/10.1016/j.jpowsour.2013.12.138.
[12] Wang P, Zhang X, Yang L, Zhang X, Yang M, Chen H, et al. Real-time monitoring of internal temperature evolution of the lithium-ion coin cell battery during the charge and discharge process. Extrem Mech Lett 2016;9:459–66. https://doi.org/10.1016/j.eml.2016.03.013.
[13] Samad NA, Siegel JB, Stefanopoulou AG, Knobloch A. Observability analysis for surface sensor location in encased battery cells. Proc Am Contr Conf 2015:299–304. https://doi.org/10.1109/ACC.2015.7170752. 2015-July:.
[14] Robinson JB, Shearing PR, Brett DJL. Thermal imaging of electrochemical power systems: a review. J Imaging 2016;2. https://doi.org/10.3390/jimaging2010002.
[15] Goutam S, Timmermans JM, Omar N, Van den Bossche P, Van Mierlo J. Comparative study of surface temperature behavior of commercial li-ion pouch cells of different chemistries and capacities by infrared thermography. Energies 2015;8:8175–92. https://doi.org/10.3390/en8088175.
[16] Cheng X, Pecht M. In situ stress measurement techniques on li-ion battery electrodes: a review. Energies 2017;10. https://doi.org/10.3390/en10050591.
[17] Wang X, Sone Y, Segami G, Naito H, Yamada C, Kibe K. Understanding volume change in lithium-ion cells during charging and discharging using in situ measurements. J Electrochem Soc 2007;154:A14. https://doi.org/10.1149/1.2386933.
[18] Cannarella J, Arnold CB. Stress evolution and capacity fade in constrained lithium-ion pouch cells. J Power Sources 2014;245:745–51. https://doi.org/10.1016/j.jpowsour.2013.06.165.
[19] Leung PK, Moreno C, Masters I, Hazra S, Conde B, Mohamed MR, et al. Real-time displacement and strain mappings of lithium-ion batteries using three-dimensional digital image correlation. J Power Sources 2014;271:82–6. https://doi.org/10.1016/j.jpowsour.2014.07.184.
[20] Louli AJ, Ellis LD, Dahn JR. Operando pressure measurements reveal solid electrolyte interphase growth to rank Li-ion cell performance. Joule 2019;3:745–61. https://doi.org/10.1016/j.joule.2018.12.009.
[21] Yu X, Feng Z, Ren Y, Henn D, Wu Z, An K, et al. Simultaneous operando measurements of the local temperature, state of charge, and strain inside a commercial lithium-ion battery pouch cell. J Electrochem Soc 2018;165:A1578–85. https://doi.org/10.1149/2.1251807jes.
[22] Hannan MA, Lipu MSH, Hussain A, Mohamed A. A review of lithium-ion battery state of charge estimation and management system in electric vehicle applications: challenges and recommendations. Renew Sustain Energy Rev 2017;78:834–54. https://doi.org/10.1016/j.rser.2017.05.001.
[23] Berecibar M, Gandiaga I, Villarreal I, Omar N, Van Mierlo J, Van Den Bossche P. Critical review of state of health estimation methods of Li-ion batteries for real applications. Renew Sustain Energy Rev 2016;56:572–87. https://doi.org/10.1016/j.rser.2015.11.042.
[24] Westerhoff U, Kroker T, Kurbach K, Kurrat M. Electrochemical impedance spectroscopy based estimation of the state of charge of lithium-ion batteries. J Energy Storage 2016;8:244–56. https://doi.org/10.1016/j.est.2016.09.001.
[25] Wang X, Wei X, Zhu J, Dai H, Zheng Y, Xu X, et al. A review of modeling, acquisition, and application of lithium-ion battery impedance for onboard battery management. ETransportation 2021;7:100093. https://doi.org/10.1016/j.etran.2020.100093.
[26] Hu X, Yuan H, Zou C, Li Z, Zhang L. Co-estimation of state of charge and state of health for lithium-ion batteries based on fractional-order calculus. IEEE Trans Veh Technol 2018;67:10319–29. https://doi.org/10.1109/TVT.2018.2865664.
[27] Deng Z, Hu X, Lin X, Xu L, Che Y, Hu L. General discharge voltage information enabled health evaluation for lithium-ion batteries. IEEE/ASME Trans Mechatronics 2020;4435. https://doi.org/10.1109/TMECH.2020.3040010.
[28] Deng Z, Hu X, Lin X, Che Y, Xu L, Guo W. Data-driven state of charge estimation for lithium-ion battery packs based on Gaussian process regression. Energy 2020;205. https://doi.org/10.1016/j.energy.2020.118000.
[29] Shu X, Shen J, Li G, Zhang Y, Chen Z, Liu Y. A flexible state of health prediction scheme for lithium-ion battery packs with long short-term memory network and transfer learning. IEEE Trans Transp Electrif 2021:7782. https://doi.org/10.1109/TTE.2021.3074638.
[30] Li Y, Li Y, Pei A, Yan K, Sun Y, Wu CL, et al. Atomic structure of sensitive battery materials and interfaces revealed by cryo–electron microscopy. Science 2017;358(80-):506–10. https://doi.org/10.1126/science.aam6014.
[31] Mehdi BL, Qian J, Nasybulin E, Park C, Welch DA, Faller R, et al. Observation and quantification of nanoscale processes in lithium batteries by operando electrochemical (S)TEM. Nano Lett 2015;15:2168–73. https://doi.org/10.1021/acs.nanolett.5b00175.
[32] Nascimento M, Ferreira MS, Pinto JL. Simultaneous sensing of temperature and bi-directional strain in a prismatic li-ion battery. Batteries 2018;4. https://doi.org/10.3390/batteries4020023.
[33] Lao J, Sun P, Liu F, Zhang X, Zhao C, Mai W, et al. In situ plasmonic optical fiber detection of the state of charge of supercapacitors for renewable energy storage. Light Sci Appl 2018;7:34. https://doi.org/10.1038/s41377-018-0040-y.
[34] Huang J, Albero Blanquer L, Bonefacino J, Logan ER, Alves Dalla Corte D, Delacourt C, et al. Operando decoding of chemical and thermal events in commercial Na(Li)-ion cells via optical sensors. Nat Energy 2020;5:674–83. https://doi.org/10.1038/s41560-020-0665-y.
[35] Nascimento M, Ferreira MS, Pinto JL. Temperature fiber sensing of Li-ion batteries under different environmental and operating conditions. Appl Therm Eng 2019;149:1236–43. https://doi.org/10.1016/j.applthermaleng.2018.12.135.
[36] Raghavan A, Kiesel P, Sommer LW, Schwartz J, Lochbaum A, Hegyi A, et al. Embedded fiber-optic sensing for accurate internal monitoring of cell state in advanced battery management systems part 1: cell embedding method and performance. J Power Sources 2017;341:466–73. https://doi.org/10.1016/j.jpowsour.2016.11.104.
[37] Ganguli A, Saha B, Raghavan A, Kiesel P, Arakaki K, Schuh A, et al. Embedded fiber-optic sensing for accurate internal monitoring of cell state in advanced battery management systems part 2: internal cell signals and utility for state estimation. J Power Sources 2017;341:474–82. https://doi.org/10.1016/j.jpowsour.2016.11.103.
[38] Grattan KTV, Meggitt BT. Optical fiber sensor technology: applications and systems. London: Kluwer Academic Publishers; 1999.
[39] Novais S, Nascimento M, Grande L, Domingues MF, Antunes P, Alberto N, et al. Internal and external temperature monitoring of a li-ion battery with fiber bragg grating sensors. Sensors 2016;16. https://doi.org/10.3390/s16091394.
[40] Cao-Paz AM, Marcos-Acevedo J, del Río-Vázquez A, Martínez-Peñalver C, Lago-Ferreiro A, Nogueiras-Meléndez AA, et al. A multi-point sensor based on optical fiber for the measurement of electrolyte density in lead-acid batteries. Sensors 2010;10:2587–608. https://doi.org/10.3390/s100402587.
[41] Du C, Zhang W S, He L M, Liu L S. Measuring device for internal temperature of lithium ion battery and measuring method. Chinese Patent: CN102052976.
[42] Yu Y, Vergori E, Worwood D, Tripathy Y, Guo Y, Somá A, et al. Distributed thermal monitoring of lithium ion batteries with optical fibre sensors. J Energy Storage 2021;39. https://doi.org/10.1016/j.est.2021.102560.
[43] Wilkinson M, Blanco M, Gu E, Martin JJ, Wilkinson DP, Zhang JJ, Wang H. In situ experimental technique for measurement of temperature and current distribution in proton exchange membrane fuel cells. Electrochem Solid State Lett 2006;9:A507. https://doi.org/10.1149/1.2338769.
[44] David NA, Wild PM, Hu J, Djilali N. In-fibre Bragg grating sensors for distributed temperature measurement in a polymer electrolyte membrane fuel cell. J Power Sources 2009;192(2):376–80. https://doi.org/10.1016/j.jpowsour.2009.03.021.
[45] David NA, Wild PM, Jensen J, Navessin T, Djilali N. Simultaneous in situ measurement of temperature and relative humidity in a PEMFC using optical fiber sensors. J Electrochem Soc 2010;157:B1173. https://doi.org/10.1149/1.3436652.
[46] Inman K, Wang X, Sangeorzan B. Design of an optical thermal sensor for proton exchange membrane fuel cell temperature measurement using phosphor thermometry. J Power Sources 2010;195:4753–7. https://doi.org/10.1016/j.jpowsour.2010.02.071.
[47] Lee CY, Fan WY, Hsieh WJ. In-situ monitoring of internal local temperature and voltage of proton exchange membrane fuel cells. Sensors 2010;10:6395–405. https://doi.org/10.3390/s100706395.
[48] Yang G, Leitão C, Li Y, Pinto J, Jiang X. Real-time temperature measurement with fiber Bragg sensors in lithium batteries for safety usage. Meas J Int Meas Confed 2013;46:3166–72. https://doi.org/10.1016/j.measurement.2013.05.027.
[49] Sommer LW, Raghavan A, Kiesel P, Saha B, Staudt T, Lochbaum A, et al. Embedded fiber optic sensing for accurate state estimation in advanced battery management systems. MRS Proc 2014;1681. https://doi.org/10.1557/opl.2014.560. mrss14-1681-q01-03.
[50] Meyer J, Nedjalkov A, Doering A, Angelmahr M, Schade W. Fiber optical sensors for enhanced battery safety. Fiber Opt Sensors Appl XII 2015;9480:94800Z. https://doi.org/10.1117/12.2183325.
[51] Nascimento M, Ferreira MS, Pinto JL. Real time thermal monitoring of lithium batteries with fiber sensors and thermocouples: a comparative study. Meas J Int Meas Confed 2017;111:260–3. https://doi.org/10.1016/j.measurement.2017.07.049.
[52] Sommer LW, Kiesel P, Ganguli A, Lochbaum A, Saha B, Schwartz J, et al. Fast and slow ion diffusion processes in lithium ion pouch cells during cycling observed with fiber optic strain sensors. J Power Sources 2015;296:46–52. https://doi.org/10.1016/j.jpowsour.2015.07.025.
[53] Osuch T, Jurek T, Markowski K, Jedrzejewski K. Simultaneous measurement of liquid level and temperature using tilted fiber bragg grating. IEEE Sensor J 2016;16:1205–9. https://doi.org/10.1109/JSEN.2015.2501381.
[54] Jiang Q, Hu D, Yang M. Simultaneous measurement of liquid level and surrounding refractive index using tilted fiber Bragg grating. Sensors Actuators, A Phys 2011;170:62–5. https://doi.org/10.1016/j.sna.2011.06.001.
[55] Moreno Y, Song Q, Xing Z, Lu T, Qin H, Sun Y, et al. Hybrid polarizing grating and TFBG based SPR refractive index sensor. In: 18th int conf opt commun networks; 2019. https://doi.org/10.1109/ICOCN.2019.8934375. ICOCN 2019 2019.

[56] Miao Y, Liu B, Zhang H, Li Y, Zhou H, Sun H, et al. Relative humidity sensor based on tilted fiber Bragg grating with polyvinyl alcohol coating. IEEE Photon Technol Lett 2009;21:441–3. https://doi.org/10.1109/LPT.2009.2013185.

[57] Lopez Aldaba A, González-Vila Á, Debliquy M, Lopez-Amo M, Caucheteur C, Lahem D. Polyaniline deposition on tilted fiber Bragg grating for pH sensing. 25th Int Conf Opt Fiber Sensors 2017;10323:103235F. https://doi.org/10.1117/12.2267524.

[58] Sun X, Du H, Dong X, Hu Y, Duan J. Simultaneous curvature and temperature sensing based on a novel mach-zehnder interferometer. Photonic Sensors 2020;10:171–80. https://doi.org/10.1007/s13320-019-0551-z.

[59] Sun M, Xu B, Dong X, Li Y. Optical fiber strain and temperature sensor based on an in-line Mach-Zehnder interferometer using thin-core fiber. Opt Commun 2012;285:3721–5. https://doi.org/10.1016/j.optcom.2012.04.046.

[60] Zhao Y, Xia F, Chen M qing. Curvature sensor based on Mach–Zehnder interferometer with vase-shaped tapers. Sensors Actuators, A Phys 2017;265:275–9. https://doi.org/10.1016/j.sna.2017.09.005.

[61] Wang Q, Wei W, Guo M, Zhao Y. Optimization of cascaded fiber tapered Mach-Zehnder interferometer and refractive index sensing technology. Sensor Actuator B Chem 2016;222:159–65. https://doi.org/10.1016/j.snb.2015.07.098.

[62] Sun M, Jin Y, Dong X. All-Fiber mach–zehnder interferometer for liquid level measurement. IEEE Sensor J 2015;15:3984–8. https://doi.org/10.1109/JSEN.2015.2406872.

[63] Lopez-Torres D, Elosua C, Villatoro J, Zubia J, Rothhardt M, Schuster K, et al. Photonic crystal fiber interferometer coated with a PAH/PAA nanolayer as humidity sensor. Sensor Actuator B Chem 2017;242:1065–72. https://doi.org/10.1016/j.snb.2016.09.144.

[64] Lei M, Zhang YN, Han B, Zhao Q, Zhang A, Fu D. In-line mach-zehnder interferometer and FBG with smart hydrogel for simultaneous pH and temperature detection. IEEE Sensor J 2018;18:7499–504. https://doi.org/10.1109/JSEN.2018.2862426.

[65] Liu Y, Wang DN, Chen WP. Crescent shaped Fabry-Perot fiber cavity for ultra-sensitive strain measurement. Sci Rep 2016;6:38390. https://doi.org/10.1038/srep38390.

[66] Wu C, Liu Z, Zhang AP, Guan B-O, Tam H-Y. In-line open-cavity Fabry–Pérot interferometer formed by C-shaped fiber fortemperature-insensitive refractive index sensing. Opt Express 2014;22:21757. https://doi.org/10.1364/oe.22.021757.

[67] Quan M, Tian J, Yao Y. Ultra-high sensitivity Fabry–Perot interferometer gas refractive index fiber sensor based on photonic crystal fiber and Vernier effect. Opt Lett 2015;40:4891. https://doi.org/10.1364/ol.40.004891.

[68] Liu Y, Yang D, Wang Y, Zhang T, Shao M, Yu D, et al. Fabrication of dual-parameter fiber-optic sensor by cascading FBG with FPI for simultaneous measurement of temperature and gas pressure. Opt Commun 2019;443:166–71. https://doi.org/10.1016/j.optcom.2019.03.034.

[69] Liu Y, Zhang T, Wang Y, Yang D, Liu X, Fu H, et al. Simultaneous measurement of gas pressure and temperature with integrated optical fiber FPI sensor based on in-fiber micro-cavity and fiber-tip. Opt Fiber Technol 2018;46:77–82. https://doi.org/10.1016/j.yofte.2018.09.021.

[70] Shi J, Xu D, Xu W, Wang Y, Yan C, Zhang C, et al. Humidity sensor based on fabry-perot interferometer and intracavity sensing of fiber laser. J Lightwave Technol 2017;35:4789–95. https://doi.org/10.1109/JLT.2017.2750172.

[71] Wu J, Yin MJ, Seefeldt K, Dani A, Guterman R, Yuan J, et al. In situ μ-printed optical fiber-tip CO2 sensor using a photocrosslinkable poly(ionic liquid). Sensor Actuator B Chem 2018;259:833–9. https://doi.org/10.1016/j.snb.2017.12.125.

[72] Costa GKB, Gouvêa PMP, Soares LMB, Pereira JMB, Favero F, Braga AMB, et al. In-fiber Fabry-Perot interferometer for strain and magnetic field sensing. Opt Express 2016;24:14690. https://doi.org/10.1364/oe.24.014690.

[73] Fan H, Zhang L, Gao S, Chen L, Bao X. Ultrasound sensing based on an in-fiber dual-cavity Fabry–Perot interferometer. Opt Lett 2019;44:3606. https://doi.org/10.1364/ol.44.003606.

[74] Hou D, Kang J, Wang L, Zhang Q, Zhao Y, Zhao C. Bare fiber adapter based Fabry-Pérot interferometer for microfluidic velocity measurement. Opt Fiber Technol 2019;50:71–5. https://doi.org/10.1016/j.yofte.2019.02.013.

[75] Liu S, Yang K, Wang Y, Qu J, Liao C, He J, et al. High-sensitivity strain sensor based on in-fiber rectangular air bubble. Sci Rep 2015;5. https://doi.org/10.1038/srep07624.

[76] Pan Y, Liu T, Jiang J, Liu K, Wang S, Yin J, et al. Simultaneous measurement of temperature and strain using spheroidal-cavity-overlapped FBG. IEEE Photonics J 2015;7. https://doi.org/10.1109/JPHOT.2015.2493724.

[77] Ferreira MS, Bierlich J, Kobelke J, Schuster K, Santos JL, Frazão O. Towards the control of highly sensitive Fabry-Pérot strain sensor based on hollow-core ring photonic crystal fiber. Opt Express 2012;20:21946. https://doi.org/10.1364/oe.20.021946.

[78] Yin MJ, Gu B, An QF, Yang C, Guan YL, Yong KT. Recent development of fiber-optic chemical sensors and biosensors: mechanisms, materials, micro/nano-fabrications and applications. Coord Chem Rev 2018;376:348–92. https://doi.org/10.1016/j.ccr.2018.08.001.

[79] Leung A, Shankar PM, Mutharasan R. A review of fiber-optic biosensors. Sensor Actuator B Chem 2007;125(2):688–703. https://doi.org/10.1016/j.snb.2007.03.010.

[80] Handali JP, Pawinanto RE, Mulyanti B, Sugandi G. Simulation of de-cladding fiber optic sensor using MODE solutions for ammonia detection. Int symp electron smart devices smart devices big data anal Mach learn. ISESD 2018; 2019. https://doi.org/10.1109/ISESD.2018.8605450.

[81] Ouyang T, Lin L, Xia K, Jiang M, Lang Y, Guan H, et al. Enhanced optical sensitivity of molybdenum diselenide (MoSe2) coated side polished fiber for humidity sensing. Opt Express 2017;25(9):9823–33. https://doi.org/10.1364/OE.25.009823.

[82] Liu D, Mallik AK, Yuan J, Yu C, Farrell G, Semenova Y, et al. High sensitivity refractive index sensor based on a tapered small core single-mode fiber structure. Opt Lett 2015;40:4166. https://doi.org/10.1364/ol.40.004166.

[83] Gowri A, Sai VVR. Development of LSPR based U-bent plastic optical fiber sensors. Sensor Actuator B Chem 2016;230:536–43. https://doi.org/10.1016/j.snb.2016.02.074.

[84] beroglu O. The determination of Listeria monocytogenes in foods with optical biosensors. Vet J 2020. https://doi.org/10.36483/vanvetj.643925.

[85] Guo S, Albin S. Transmission property and evanescent wave absorption of cladded multimode fiber tapers. Opt Express 2003;11:215. https://doi.org/10.1364/oe.11.000215.

[86] Iyer K. Development of multifunctional fiber optic sensors for lithium ion-battery monitoring. 2016.

[87] Liang G, Luo Z, Liu K, Wang Y, Dai J, Duan Y. Fiber optic surface plasmon resonance–based biosensor technique- fabrication, advancement, and application. Crit Rev Anal 2016;46(3):213–23. https://doi.org/10.1080/10408347.2015.1045119.

[88] Fujimoto S, Uemura S, Imanishi N, Hirai S. Oxygen concentration measurement in the porous cathode of a lithium-air battery using a fine optical fiber sensor. Mech Eng Lett 2019;5. https://doi.org/10.1299/mel.19-00095. 19-00095-19–00095.

[89] Ding Z, Wang C, Liu K, Jiang J, Yang D, Pan G, et al. Distributed optical fiber sensors based on optical frequency domain reflectometry: a review. Sensors 2018;18. https://doi.org/10.3390/s18041072.

[90] Bao X, Chen L. Recent progress in Brillouin scattering based fiber sensors. Sensors 2011;11:4152–87. https://doi.org/10.3390/s110404152.

[91] Lu P, Lalam N, Badar M, Liu B, Chorpening BT, Buric MP, et al. Distributed optical fiber sensing: review and perspective. Appl Phys Rev 2019;6. https://doi.org/10.1063/1.5113955.

[92] Barrias A, Casas JR, Villalba S. A review of distributed optical fiber sensors for civil engineering applications. Sensors 2016;16. https://doi.org/10.3390/s16050748.

[93] Schenato L. A review of distributed fibre optic sensors for geo-hydrological applications. Appl Sci 2017;7. https://doi.org/10.3390/app7090896.

[94] Ramakrishnan M, Rajan G, Semenova Y, Farrell G. Overview of fiber optic sensor technologies for strain/temperature sensing applications in composite materials. Sensors 2016;16. https://doi.org/10.3390/s16010099.

[95] Chow DM, Thevenaz L. Opto-acoustic chemical sensor based on forward stimulated Brillouin scattering in optical fiber. In: IEEE 7th int conf photonics; 2018. https://doi.org/10.1109/ICP.2018.8533216. ICP 2018 2018.

[96] Fleming J, Amietszajew T, McTurk E, Greenwood D, Bhagat R. Development and evaluation of in-situ instrumentation for cylindrical Li-ion cells using fibre optic sensors. HardwareX 2018;3:100–9. https://doi.org/10.1016/j.ohx.2018.04.001.

[97] Vergori E, Yu Y. Monitoring of Li-ion cells with distributed fibre optic sensors. Procedia Struct Integr 2019;24:233–9. https://doi.org/10.1016/j.prostr.2020.02.020.

[98] Bae CJ, Manandhar A, Kiesel P, Raghavan A. Monitoring the strain evolution of lithium-ion battery electrodes using an optical fiber bragg grating sensor. Energy Technol 2016;4:851–5. https://doi.org/10.1002/ente.201500514.

[99] Fortier A, Tsao M, Williard ND, Xing Y, Pecht MG. Preliminary study on integration of fiber optic bragg grating sensors in li-ion batteries and in situ strain and temperature monitoring of battery cells. Energies 2017;10. https://doi.org/10.3390/en10070838.

[100] Peng J, Zhou X, Jia S, Jin Y, Xu S, Chen J. High precision strain monitoring for lithium-ion batteries based on fiber Bragg grating sensors. J Power Sources 2019;433:226692. https://doi.org/10.1016/j.jpowsour.2019.226692.

[101] Nedjalkov A, Meyer J, Gräfenstein A, Schramm B, Angelmahr M, Schwenzel J, et al. Refractive index measurement of lithium ion battery electrolyte with etched surface cladding waveguide bragg gratings and cell electrode state monitoring by optical strain sensors. Batteries 2019;5. https://doi.org/10.3390/batteries5010030.

[102] Vidakovic M, Rente B, Fabian M, Li X, Fisher P, Li K, et al. Flow measurement inside a zinc-nickel flow cell battery using FBG based sensor system. EWOFS 2019;49. https://doi.org/10.1117/12.2539875.

[103] Ghannoum A, Norris RC, Iyer K, Zdravkova L, Yu A, Nieva P. Optical characterization of commercial lithiated graphite battery electrodes and in situ fiber optic evanescent wave spectroscopy. ACS Appl Mater Interfaces 2016;8:18763–9. https://doi.org/10.1021/acsami.6b03638.

[104] Ghannoum A, Iyer K, Nieva P, Khajepour A. Fiber optic monitoring of lithium-ion batteries: a novel tool to understand the lithiation of batteries. Proc IEEE Sensors 2017. https://doi.org/10.1109/ICSENS.2016.7808695.

[105] Ghannoum A, Nieva P, Yu A, Khajepour A. Development of embedded fiber-optic evanescent wave sensors for optical characterization of graphite anodes in lithium-ion batteries. ACS Appl Mater Interfaces 2017;9:41284–90. https://doi.org/10.1021/acsami.7b13464.

[106] Ghannoum AR, Nieva P. Graphite lithiation and capacity fade monitoring of lithium ion batteries using optical fibers. J Energy Storage 2020;28. https://doi.org/10.1016/j.est.2020.101233.

[107] Modrzynski C, Roscher V, Rittweger F, Ghannoum AR, Nieva P, Riemschneider KR. Integrated optical fibers for simultaneous monitoring of the anode and the cathode in lithium ion batteries. Proc IEEE Sensors 2019. https://doi.org/10.1109/SENSORS43011.2019.8956755. 2019-October.

[108] Qian S, Chen X, Jiang S, Pan Q, Gao Y, Wang L, et al. Direct detection of charge and discharge process in supercapacitor by fiber-optic LSPR sensors. Nanophotonics 2020;9:1071–9. https://doi.org/10.1515/nanoph-2019-0504.

[109] Ma CT. A novel state of charge estimating scheme based on an air-gap fiber interferometer sensor for the vanadium redox flow battery. Energies 2020;13. https://doi.org/10.3390/en13020291.
[110] Fleming J, Amietszajew T, Charmet J, Roberts AJ, Greenwood D, Bhagat R. The design and impact of in-situ and operando thermal sensing for smart energy storage. J Energy Storage 2019;22:36–43. https://doi.org/10.1016/j.est.2019.01.026.
[111] Hedman J, Nilebo D, Larsson Langhammer E, Björefors F. Fibre optic sensor for characterisation of lithium-ion batteries. ChemSusChem 2020;13:5731–9. https://doi.org/10.1002/cssc.202001709.
[112] Vehicle INL. Testing | advanced vehicle testing activity. 2021. accessed, https://avt.inl.gov/content/vehicle-testing. [Accessed 27 June 2021].
[113] NFPA. Alternative fuel vehicle (AFV) safety training. NFPA; 2021. accessed, http://www.evsafetytraining.org/resources/auto-manufacturer-resources.aspx. [Accessed 27 June 2021].
[114] Hardware NEC. Details - NEC energy solutions. 2021. accessed, https://www.neces.com/solutions/hardware-details/. [Accessed 27 June 2021].
[115] Tesla. Powerpack – commercial & utility energy storage solutions | tesla. 2021. accessed, https://www.tesla.com/powerpack. [Accessed 27 June 2021].
[116] Dai H, Jiang B, Hu X, Lin X, Wei X, Pecht M. Advanced battery management strategies for a sustainable energy future: multilayer design concepts and research trends. Renew Sustain Energy Rev 2021;138:110480. https://doi.org/10.1016/j.rser.2020.110480.
[117] Lu L, Han X, Li J, Hua J, Ouyang M. A review on the key issues for lithium-ion battery management in electric vehicles. J Power Sources 2013;226:272–88. https://doi.org/10.1016/j.jpowsour.2012.10.060.
[118] Hossain Lipu MS, Hannan MA, Karim TF, Hussain A, Saad MHM, Ayob A, et al. Intelligent algorithms and control strategies for battery management system in electric vehicles: progress, challenges and future outlook. J Clean Prod 2021:292. https://doi.org/10.1016/j.jclepro.2021.126044.
[119] Wei Z, Zhao J, He H, Ding G, Cui H, Liu L. Future smart battery and management: advanced sensing from external to embedded multi-dimensional measurement. J Power Sources 2021;489:229462. https://doi.org/10.1016/j.jpowsour.2021.229462.